energies

MDPI

Article

Swirl-Bypass Nozzle for CO_2 Two-Phase Ejectors: Numerical Design Exploration

Knut Emil Ringstad [1,*], Krzysztof Banasiak [2], Åsmund Ervik [2] and Armin Hafner [1,*]

[1] Department of Energy and Process Engineering, Norwegian University of Science and Technology, Kolbjørn Hejes vei 1B, 7491 Trondheim, Norway
[2] SINTEF Energy Research, Kolbjørn Hejes vei 1d, 7465 Trondheim, Norway
* Correspondence: knutringstad@gmail.no (K.E.R.); armin.hafner@ntnu.no (A.H.)

Abstract: In this work, a novel ejector design concept of a swirl-bypass nozzle is proposed to improve off-design performance of CO_2 two-phase ejectors. The swirl-bypass nozzle allows part of the flow to bypass into the ejector mixing chamber to generate swirl. The design of such a device is investigated using a 3D multiphase CFD model. An extensive experimental test campaign is conducted to validate the baseline homogeneous equilibrium CFD model. The model's prediction motive mass flow rate within 2–12% error and suction mass flow rate was predicted with 3–50% error. Based on the tested ejector geometry, simulations of different ejector swirl-bypass inlets are conducted. The results show that, for the current design, total entrainment of the ejector is reduced by 2–20% with the swirl-bypass inlet. The axial position of the bypass inlet plays a primary role in the bypass inlet flow rate, and, consequently, in suction flow reduction. This is found to be due to the bypass flow blocking off the suction mass flow rate, which has a net negative impact on performance. Finally, several design improvements to improve future designs are proposed.

Keywords: computational fluid dynamics; two-phase ejector; CO_2; bypass ejector; swirl bypass

Citation: Ringstad, K.E.; Banasiak, K.; Ervik, Å.; Hafner, A. Swirl-Bypass Nozzle for CO_2 Two-Phase Ejectors: Numerical Design Exploration. *Energies* **2022**, *15*, 6765. https://doi.org/10.3390/en15186765

Academic Editor: Vasily Novozhilov

Received: 21 August 2022
Accepted: 12 September 2022
Published: 16 September 2022

1. Introduction

1.1. Literature Review

Environmentally friendly heating and cooling solutions have seen a large growth in recent years. With the ratification of the EU F-gas legislation and the Kigali amendment to the Montreal Protocol [1], increased efforts have been put toward the development of efficient and environmentally friendly cooling and heat-pumping systems. Due to the rapid transition to environmentally friendly refrigerants, much research has been put toward finding efficient system solutions with natural working fluids, such as ammonia, water, hydrocarbons, and CO_2.

A promising natural working fluid for many applications is CO_2 (R744). CO_2-based refrigeration and heat-pumping systems have been applied for many applications, such as supermarkets [2,3], heat-pump units [4–6], vehicles [7–9], light commercial refrigeration [10,11], tumble dryers [12,13], chillers [14], air-conditioners [15], and integrated systems for hotels [16]. As a refrigerant, CO_2 has several beneficial characteristics, such as favorable thermodynamic properties that allow for smaller components and efficient refrigeration cycles. Furthermore, CO_2 is non-toxic, non-flammable, and has a negligible GWP of one while being cheap and widely available [17].

However, the high operating pressure of the CO_2 transcritical cycle is associated with increased expansion losses. These losses can be partially recovered by implementing work-recovery devices such as two-phase ejectors. Ejectors work by using the expansion energy of the high-pressure flow (motive flow) and expand the flow through a super-sonic converging-diverging nozzle. The high-velocity motive flow is then mixed with a secondary flow (suction flow) and the mixture is repressurized by slowing the flow down in a diffuser.

This effectively pumps the suction flow to a higher pressure without additional work, improving system efficiency. Ejector performance is, therefore, commonly evaluated using the ratio of pumped suction mass flow rate to motive mass flow rate (Equation (1)), referred to as the entrainment ratio of the ejector.

$$\omega = \mathrm{MFR}_{\mathrm{suction}} / \mathrm{MFR}_{\mathrm{motive}} \quad (1)$$

Two-phase R744 (CO_2) ejectors are today implemented in several cooling and heat-pump applications [18–28], and can improve system COP by 10–30% [19,29].

The promising benefits of using ejector-supported R744 systems have promoted much research into ejector design and operation. Due to the complex fluid dynamics within these components, much experimental and numerical research has been devoted to better the understanding of multiphase ejectors and their design. Accurate numerical models are of high value for R744 ejector design due to several reasons, such as high sensitivity to small changes in its many design parameters, the high cost of the experimental testing of ejectors, the large differences in optimal design for different applications, and the possibility of performing low-cost exploratory investigations into their design. This has prompted research into advanced models for R744 ejectors, such as the 0D and 1D models [30–35], which have been applied for system-level calculations and ejector design. A limitation of numerical modeling using thermodynamic or 1D approaches is their inability to generally predict phenomena such as flow separation or shock-wave patterns. This problem becomes important when exploring novel ejector designs. Furthermore, new geometric ejector designs that are not within conventional ejector design space are not possible to investigate with such approaches. In recent years, emphasis has been put toward developing accurate and fast multiphase computational fluid dynamics (CFD) models for R744 ejectors, where the full 2D or 3D ejector physics are resolved, allowing for more exploratory investigations of ejector designs. Accurate CFD modeling has the added benefit of allowing detailed insights into ejector physics as all flow variables are available. However, these models are, in general, more complex and more computationally costly.

The most prominent model used in R744 two-phase ejectors modeling is the homogeneous equilibrium models (HEM) [36–44]. In general, for high-pressure and temperature motive conditions, the HEM provides good prediction accuracy at a low computational cost. However, as the motive pressure and temperature are reduced, non-equilibrium effects are no longer negligible, and delayed phase transition must be considered. Several models have been presented in the literature to model the transition to equilibrium, such as homogeneous relaxation models [40,45,46], and mixture models [47–50]. These models treat transition by considering a delayed time scale to reach equilibrium, or by modeling the phase change mechanisms directly. Non-equilibrium models have better predictive capabilities than equilibrium-based approaches for motive operating conditions in the "off-critical" region (i.e., $T_m \lesssim 30$ °C, $P_m \lesssim 75$ bar) [51]. Accurate prediction of R744 ejector flow is still an ongoing research area. Significant uncertainties are also associated with the prediction of the secondary ejector flow. This is considered a consequence of the lack of detailed understanding of the suction entrainment process, its dependency on accurate motive flow conditions, and the complexity of the multiphase turbulent mixing process in the ejector. For detailed reviews of the current status of R744 two-phase ejector modeling, see Ringstad et al. [51] and Nowak et al. [52]. Extensive experimental tests are needed to validate and verify the numerical models. Detailed experimental observations of R744 ejectors are limited, even though some work has been carried out on visualization and local measurements [53–55], additional experimental results with varied and open-access ejector geometries are needed.

A primary reason for the large interest in ejector modeling is the necessity for a detailed understanding of ejector design and its impact on ejector performance under varied operating conditions, which has been highlighted as a key focus area for ejector developments [19,51,52]. Several studies on R744 ejector design have been conducted to better understand the interdependence of different design parameters [29,44,56]. Improved

ejector-design processes have been explored using numerical CFD modeling in combination with optimization techniques. Palacz et al. [38,39] combined an evolutionary optimization algorithm with CFD modeling to optimize ejector design. Ringstad et al. [57] presented a machine-learning-based design methodology for the ejector design and performance mapping of R744 ejectors.

An efficient ejector design is highly dependent on the system operating conditions. When operated at off-design operating conditions, a passive (no active control) ejector system can dramatically reduce system COP. Nakagawa et al. [29] reported between a 34 to 82% drop in system COP for an ejector system operated in off-design conditions. Similarly, Lucas and Koehler [58] reported a 10 to 17% drop in system performance of an ejector-based system at off-design conditions. Therefore, ejector control is important for system performance. Different capacity control strategies using R744 ejectors have been presented in the literature; for a detailed review, see Gullo et al. [59]. The main technologies for this application are the multiblock ejector [60], motive swirl control [61], adjustable needle control [33,62], and pulse-width modulation [63].

Alternatively, ejector performance can be improved by active control of the suction flow. One such design is the suction-bypass design, where a controllable secondary suction inlet downstream from along the mixing section is implemented for off-design performance improvement. This inlet splits the suction flow within the ejector so that parts of the flow bypass parts of the mixing section. This allows for the suction flow to enter the ejector in a low-pressure zone under off-design conditions. The bypass concept improves ejector performance by reducing entropy production in supersonic shocks and allows for more optimal suction inflow conditions. In such designs, the entrainment ratio is defined by the total mass flow rate pumped by the recovered work from the motive flow, Equation (2):

$$\omega = (\mathrm{MFR}_{\mathrm{suction}} + \mathrm{MFR}_{\mathrm{bypass}})/\mathrm{MFR}_{\mathrm{motive}} \quad (2)$$

The goal of such a design is to increase the total pumped mass flow beyond what can be achieved with only the suction port. The bypass concept for ejectors has been investigated with various working fluids, with steam [64,65], methane [66,67], air [68,69], and R744 [70,71]. Tang et al. [65] investigated the bypass concept for steam ejectors using numerical CFD calculations. The study identified several low-pressure zones that could be utilized, and close to a 4% improvement in entrainment ratio was obtained by implementing the bypass nozzle. The bypass concept was implemented for pressure regulation in the steam ejector [65], and findings indicate an increase in entrainment ratio of up to 26% using this strategy. Chen et al. [68] presented a CFD investigation into the bypass ejector concept for air ejectors, finding that up to a 10% increased entrainment ratio could be generated. Later, Chen et al. [69] presented additional numerical results with different geometries for the bypass inlet. They found that significant improvements by up to 32.8% in entrainment ratio could be made by optimization of the bypass geometry parameters. Chen et al. [66] investigated an ejector study with methane as the working fluid where an ejector with an adjustable needle and bypass inlet was implemented, achieving up to 74.5% improved entrainment. Chen et al. [67] followed this with a detailed investigation of the methane ejector with two bypass inlets. With one bypass inlet, up to a 34.8% improvement was obtained in comparison to without a bypass. By the implementation of two bypass ports, a larger improvement of up to 48.9% was achieved. While the findings with single-phase ejectors are valuable for comparison, much of the knowledge is not directly transferable to two-phase ejectors such as those predominantly implemented in R744 cycles.

The bypass concept for R744 two-phase ejectors was first proposed and explored numerically by Bodys et al. [70]. They explored different bypass geometries using a 2D CFD model. The exploration was performed with six bypass locations in the ejector diffuser and with two bypass inlet angles at different pressure lift conditions. Their findings were that the bypass inlet could improve suction mass flow rate at low-pressure lifts by up to 37%. Furthermore, they found that the optimal location for the bypass inlet was at a distance of 40% of the mixing chamber into the diffuser. Recently, Bodys et al. [71] followed up this

study with an experimental investigation of a bypass suction inlet. In this work, the authors proved the applicability of the suction-bypass concept for ejector efficiency improvement and proposed a control strategy for such solutions. The resulting efficiency improvement was as high as 37% at low-pressure lifts when the bypass inlet was introduced. Furthermore, a full 3D CFD investigation was conducted to gain a better understanding of the ejector flow physics. The authors mention the potential for introducing a swirl component to the model for further improvements of the bypass concept.

The concept of adding the swirl component to the motive and suction flow at the ejector inlets has been proposed in previous works to intensify the mixing process in the mixing section of the ejector [72,73]. The idea is that the surface area of the interface between the suction and motive flow is increased and more momentum is transferred. Additionally, the centrifugal force can encourage faster spreading and, therefore, mixing of the central flow core. Bodys et al. [73] investigated the effects of the swirl-flow component at the ejector motive and suction inlets of a two-phase R744 ejector. They concluded that some improvements could be gained in the entrainment ratio by the implementation of a motive inlet swirl component. However, the suction flow swirl component only limited the suction flow rate through the suction nozzle and had a negative impact on the entrainment ratio. In the mentioned study, as the swirl component was added before the suction inlet, the impact of the swirl component in the mixing chamber was reduced.

1.2. Swirl-Bypass Concept

To the best of the authors' knowledge, the concept of ejector improvement through combined bypass flow and swirl generation has not been considered. In this paper, such a solution is presented and discussed in terms of its design and flow characteristics. The novel swirl-bypass concept is presented in this paper to potentially cover two applications: (A) improving entrainment ratio at off-design operating conditions and (B) serving as an additive motive-capacity control technique. These applications are illustrated in Figure 1A,B. In this work, concept (A) is investigated.

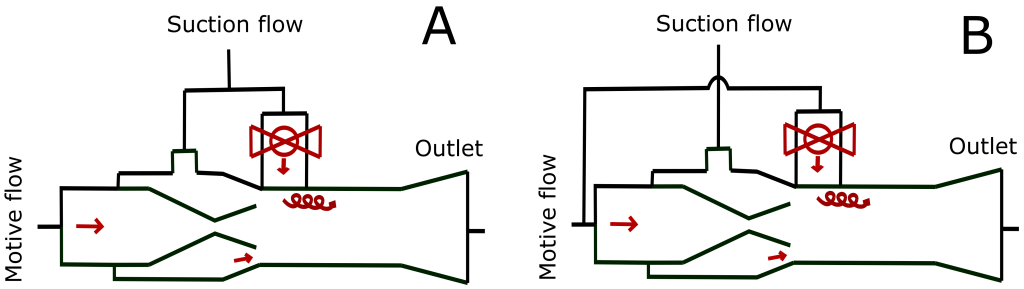

Figure 1. Illustration of the two swirl-bypass concepts (**A**,**B**). Concept (**A**) is a suction swirl bypass ejector. Concept (**B**) is a motive swirl bypass ejector.

The novel idea is to add an additional angled inlet to the ejector downstream of the motive nozzle to generate swirl flow. At off-design conditions, the inlet can be used to bypass a part of the suction flow, similar to the standard bypass inlet, and the flow can be used to generate swirl. The swirl-inducing suction flow could then potentially improve mixing efficiency, indirectly and directly improving the entrainment ratio. This corresponds to concept (A).

Alternatively, the swirl-bypass inlet can be used to control the motive mass flow rate. Similar to the motive swirl control mechanism presented by Zhu and Elbel [61], the high-pressure motive flow can be split into two streams. One stream enters the motive nozzle normally, while, unlike the motive swirl control discussed by Zhu and Elbel [61], the second stream enters the swirl-bypass entrance inside the ejector mixing chamber. The second motive flow is then used to generate swirling flow and can be controlled by a valve upstream of the bypass inlet, corresponding with concept B. Such a design allows for the

control of the motive flow not only to reduce the motive flow below the choked design value but also to increase the motive mass flow by bypassing the motive nozzle to generate swirl. This concept will perform better than a parallel expansion valve as long as the swirl flow has any positive impact on the flow.

1.3. Knowledge Gap

In this work, the novel concept of a swirl-inducing bypass inlet is explored numerically using 3D CFD simulation. As limited comparable ejector designs are available, the design space of such a bypass inlet will be tested with varied bypass geometries. Different inclination angles and locations of the bypass chamber are explored. The flow structure and its implications on ejector operation and design are discussed in terms of swirl and mixing. The results indicate that the design of this type of ejector is complex, and must be considered in conjunction with the rest of the ejector design. This study will, in this way, enable future designs of a swirl-bypass inlet and several design considerations and suggestions are presented. Limited knowledge regarding the influence of swirl on two-phase ejectors is available; however, the potential of utilizing swirl in ejectors has been highlighted by several authors in the literature [61,71]. This article further fills this knowledge gap by supplying detailed simulation results and analysis of the influence and decay of swirl in the ejector. Furthermore, the baseline HEM CFD model without a bypass is validated against new experimental results with an ejector geometry designed for high entrainment at low-pressure lift.

2. CFD Model

2.1. Multiphase Model

The CFD model used in this work is a homogeneous equilibrium model (HEM) based on the formulation by Smolka et al. [36]. The HEM assumes that both phases are at full mechanical, thermal, and thermodynamic equilibrium; hence, the flow can be described using a single velocity- ($\vec{u}$), temperature- (T), and pressure-field (P). The HEM is, therefore, classified as a pseudo-fluid or single-fluid approach where a single set of transport equations, Equations (3)–(5), are solved. Here, the energy equation, Equation (5), is reformulated to an equivalent enthalpy formulation.

$$\frac{\partial}{\partial t}\rho_{\text{mix}} + \nabla \cdot (\rho \vec{u}) = 0, \tag{3}$$

$$\frac{\partial}{\partial t}\rho_{\text{mix}}\vec{u} + \nabla \cdot (\rho \vec{u}\vec{u}) = -\nabla \cdot p + \nabla \cdot \tau_{\text{eff}}, \tag{4}$$

$$\frac{\partial}{\partial t}\rho_{\text{mix}} h_{\text{mix}} + \nabla \cdot (\rho \vec{u} h_{\text{mix}}) = \nabla \cdot (\Gamma_{\text{eff}} \nabla h_{\text{mix}}) + \dot{S}_{h1} + \dot{S}_{h2} + \dot{S}_{h3} \tag{5}$$

Here, the subscript *mix* indicates the pseudo-fluid mixture properties. ρ, p, h, q refer to the density, pressure, enthalpy, and heat flux, respectively. The effective stress tensor $\tau_{ij,\text{eff}}$ is the laminar (Newtonian) and turbulent stress tensors combined, $\tau_{\text{eff}} = \tau_{\text{laminar}} + \tau_{\text{turb}}$. In this equation, h is the specific enthalpy, and Γ_{eff} is the effective diffusion coefficient. The terms $\dot{S}_{h1,2,3}$ describe the mechanical energy, the irreversible dissipation of the kinetic energy variations, and the dissipation of the turbulent kinetic energy, respectively, explained in detail in the work by Smolka et al. [36].

The enthalpy and pressure can then be used to uniquely identify the thermodynamic equilibrium state, and, from this, the thermodynamic properties can be calculated. Properties are typically divided into thermophysical (Equation (6)) and transport (Equation (7)) properties.

$$\begin{bmatrix} \rho \\ c_p \\ \alpha \\ T \\ s \end{bmatrix} = f(p, h), \tag{6}$$

$$\begin{bmatrix} \mu \\ \lambda \end{bmatrix} = g(p,h), \tag{7}$$

where $\rho, \alpha, \mu, \lambda, c_p, s$ are the pseudo-fluid density, vapor volume fraction, kinematic viscosity, thermal conductivity, heat capacity, and entropy, respectively. Mixture properties are evaluated using mass- and volume-weighted averages.

The properties of liquid and gas are evaluated by the pressure and enthalpy, interpolated from a look-up table. The CoolProp library [74] for R744 is based on the Span–Wagner equation of state, which is considered the most accurate equation of state (EoS) for CO_2 and is widely used for R744 ejector simulations [51]. Here, CoolProp is used to generate the look-up tables that are imported in Fluent using UDFs.

The HEM model for R744 two-phase ejectors is considered accurate for motive flow inlet conditions at supercritical pressure and temperatures, referred to as "near-critical" conditions [51]. In the present study, the operating conditions will primarily concern high pressure and temperature operating conditions, where the assumption of equilibrium flow is considered fair [46]. Compared to other approaches presented in the literature, the HEM model is preferable in robustness and stability. Numerical stability is critical for modeling the complex geometry considered in this work. The HEM model has been extensively validated for R744 two-phase ejectors [51] in terms of mass flow rate predictions. Still, the prediction uncertainty of local variables, such as pressures and velocities, is not well-understood due to the lacking experimental validation data. Due to the high accuracy in the considered domain and superior stability characteristics, the HEM model is chosen for this work.

2.2. Turbulence Model

Turbulence modeling is a key feature of accurate CFD predictions. The mixing process inside the ejector is, to a large extent, governed by the turbulent viscosity, ν_t, predicted by the turbulence model. For R744 two-phase ejectors, it is common to use pseudo-fluid two-equation turbulence models, such as the $k-\epsilon$ and $k-\omega$ models. The turbulent viscosity, ν_t, can then be calculated based on two turbulence parameters. The models involve solving the set of transport equations for these turbulent properties. As studied by Bodys et al. [50], different turbulence models can yield significantly different predictions of turbulent flow characteristics. An initial study was conducted to compare the $k-\epsilon$ and $k-\omega$ models for the swirl bypass inlet geometry, discussed in Section 4.4. Due to the complexity of the geometry and sharp gradients near the bypass inlet, a fully wall-resolved simulation with turbulent mesh resolution of $y^+ \approx 1$ was not achievable and unstable simulations would occur. Instead, the mesh was resolved to $y^+ \approx 30+$. In conclusion, the $k-\omega$ SST model is used due to its better accuracy.

2.3. Numerical Approach

The CFD problem is solved using a 3D steady-state pressure-based coupled algorithm in ANSYS Fluent 2020 R2. The numerical schemes used were the second-order upwind scheme for the momentum, density, enthalpy (UDS), and turbulence transport equations. Second-order schemes were chosen to reduce the influence of numerical viscosity, while higher order discretizations were disregarded due to numerical stability concerns near the swirl bypass inlet. Higher order accuracy will improve gradient estimation, which has an impact on shock resolution. The pressure was calculated using the PRESTO! scheme, which is the preferred pressure discretization for high swirl flows [75]. Gradients were evaluated with the least-square cell gradient calculation, which is associated with comparable or higher accuracy than the Green Gauss node- and cell-based approaches, respectively, for regions of high mesh non-orthogonality [75]. This is primarily a concern in the vicinity of the swirl-bypass inlet, as the baseline mesh has otherwise high orthogonal quality. The boundary conditions were specified as pressure inlets and outlets. Constant pressure and enthalpy were specified at the inlets. These boundary conditions are standard for CFD modeling of two-phase R744 ejectors [51], and ensure that the modeling problem is well-

posed. These boundary conditions are set according to the experimentally measured values; thus, measurement uncertainty limits the accuracy of the model prediction. The turbulence boundary conditions were set to 5% turbulence intensity and a turbulent viscosity ratio of 5. The performance impact of turbulent boundary conditions is commonly found to be negligible [50] due to the turbulence generated in the ejector typically being more significant than the inlet turbulence.

2.4. Calculation of Ejector Parameters

Different ejector parameters will be investigated in this study to better understand the ejector flow structure. To evaluate the effects on ejector mixing-layer thickness, the vorticity thickness, δ_w, is used [76]:

$$\delta_w(\theta) = \Delta U_\infty / \left(\frac{\partial u_x}{\partial r} \right)_{\max} \tag{8}$$

The calculation is based on defining the thickness by the largest gradient in the mixing layer compared to the velocity difference across the boundary. The velocity difference, ΔU_∞, is calculated from:

$$\Delta U_\infty = U_{\text{motive}} - U_{\text{suction}}, \tag{9}$$

where U_{motive} is calculated based on the maximum velocity of the motive flow, and U_{suction} is calculated based on the velocity in the section between the upper boundary layer and the motive core. The characteristic velocity was, for this region, calculated based on the velocity at $r_s = 0.9 \cdot R_{\text{wall}}$.

3. Swirl Injection Geometry

The swirl-bypass inlet is an additional inlet entering the mixing chamber of the ejector. As opposed to the standard bypass inlet, the novel swirl-bypass nozzle is angled with a tangential component to the ejector. The effect of such a design is investigated in detail in this study. Several studies have shown that positive efficiency effects can be gained by increasing mixing by the use of swirl flow. To the best of the author's knowledge, the bypass injection for swirl generation in ejectors has not yet been explored in the literature. For this design, a compromise has to be made between moving the swirl-bypass inlet downstream for better off-design performance or upstream in the mixing chamber for optimal mixing performance. This is studied further in this work.

Different bypass swirl designs are possible, such as implementing a swirl chamber where the swirl is generated before being sucked into the ejector. However, in this work, a design where the bypass channel is directly inserted tangentially into the mixing chamber is explored.

The swirl-bypass port is illustrated with the main parameters shown in Figure 2. These parameters are: the relative bypass location measured from the nozzle exit position, $x_b = (x_{\text{bypass inlet}} - x_{\text{motive outlet}})/D_{\text{mix}}$; the bypass inlet width W and length L; the bypass tangential angle α_t and the bypass inclination angle α_i. The tangential angle, α_t, is the angle formed in the cross-sectional plane of the mixing chamber (y–z—cross section in Figure 2) between the center line of the bypass inlet and the radial vector from the mixing-chamber center at their intersecting point. This angle can vary between 0° and 90°, where 0° corresponds to a bypass with no tangential component and 90° corresponds to a fully tangential inlet. The bypass inclination angle is the angle between the mixing chamber centerline and the bypass inlet in the axial direction. In the suction nozzle, the suction flow is slightly expanded through a converging channel. This converts a part of the suction pressure into velocity. Similarly, a compression ratio, $CR = A_{\text{in}}/A_{\text{out}}$, is used to correct the bypass-inlet area. This area must also be corrected for the larger area on the cylindrical mixing chamber surface. The area correction is then added to the inlet of the suction bypass nozzle. Due to the tangential angle of bypass entrance, the problem is inherently three dimensional and will, in this study, be investigated with 3D CFD modeling. Here, the integration of suction and bypass ports is not considered and is left for future studies.

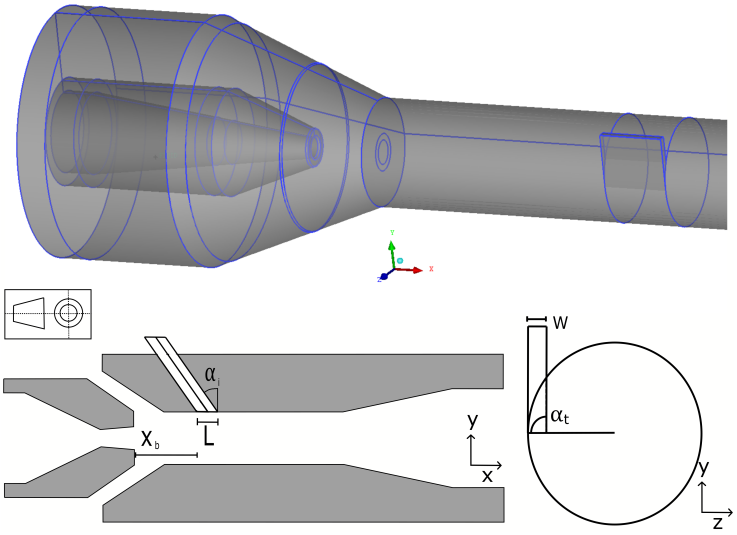

Figure 2. Generic ejector geometry with geometry parameters. Gray color signifies solid parts.

The bypass inlet dimension was defined with a length $L = D_{mix/2}$ and a width $W = D_{mix}(1 - cos(30°))/2$, such that 30° of the mixing-chamber circumference would be open. These numbers were chosen based on an initial calculation, where it was found that a larger width would limit the swirl production as a significant amount of flow would be angled toward the ejector center line with a minimal tangential component. The ejector geometry that this inlet is tested with is the geometry presented in Table 1 and was experimentally tested and numerically validated in this article. This was chosen to have a fair model validation for the baseline geometry and to compare any performance improvement or reduction with an already optimized design. However, it is noted that performance improvements are believed to be better for an ejector designed for higher pressure lift and lower entrainment ratio, discussed further in Section 6.

Table 1. Main dimensions of the ejector geometry with dimensions as defined in Ringstad et al. [57].

Parameter	D_{throat}	L_{mch}	L_{mix}	D_{mix}	D_{out}	α_{diff}	$\alpha_{m\text{-}conv}$	$\alpha_{suction}$
Value	0.85 mm	3 mm	34 mm	3.1 mm	10 mm	5°	30°	38°

4. Model Validation

The HEM has been previously extensively studied for two-phase R744 ejectors [36,46,77]. In general, the accuracy is considered to be within 5% for motive mass flow rate and 10–20% for suction mass flow rate [51] when near super-critical motive conditions are considered. Further validation and mesh independence verification are conducted with new experimental data in the following sections.

4.1. Experimental Test Campaign

To validate the 3D HEM model results, an experimental test campaign was set up at the NTNU/SINTEF Energy Research laboratory in Trondheim-Norway. The experimental rig is an R744 system with one base-load compressor and two parallel compressors, two R744 gas-coolers for heat rejection to a glycol- and a water loop, two evaporators, and an expansion device test section where a novel ejector design is installed. The detailed system description can be found in the work by Banasiak et al. [78]. The system is equipped with pressure-, temperature-, and mass-flow sensors, shown in Table 2.

Table 2. Characteristics of the measuring devices.

Parameter	Device	Accuracy
P	Cerabar PMP71	±0.25% of span
ΔP	Deltabar PMD75	±0.25% of span
T	PT 1000	±0.15 K
MFR	Rheonik RHM 08 Coriolis mass flow meter	±0.1% of reading

The system has been installed with a novel R744 two-phase ejector designed for low-pressure lift and high entrainment ratio intended for heat pump conditions. The main ejector-shape design parameters are listed in Table 1. These ejector dimensions were based on a design optimization using an advanced 1D ejector model [79]. The ejector was produced in stainless steel with a provided wall-roughness estimate of Ra0.8. To evaluate ejector performance additional pressure, temperature and mass-flow rate sensors were installed as displayed in Figure 3. The full range of experimental test points is shown in Table A1 in the Appendix A.

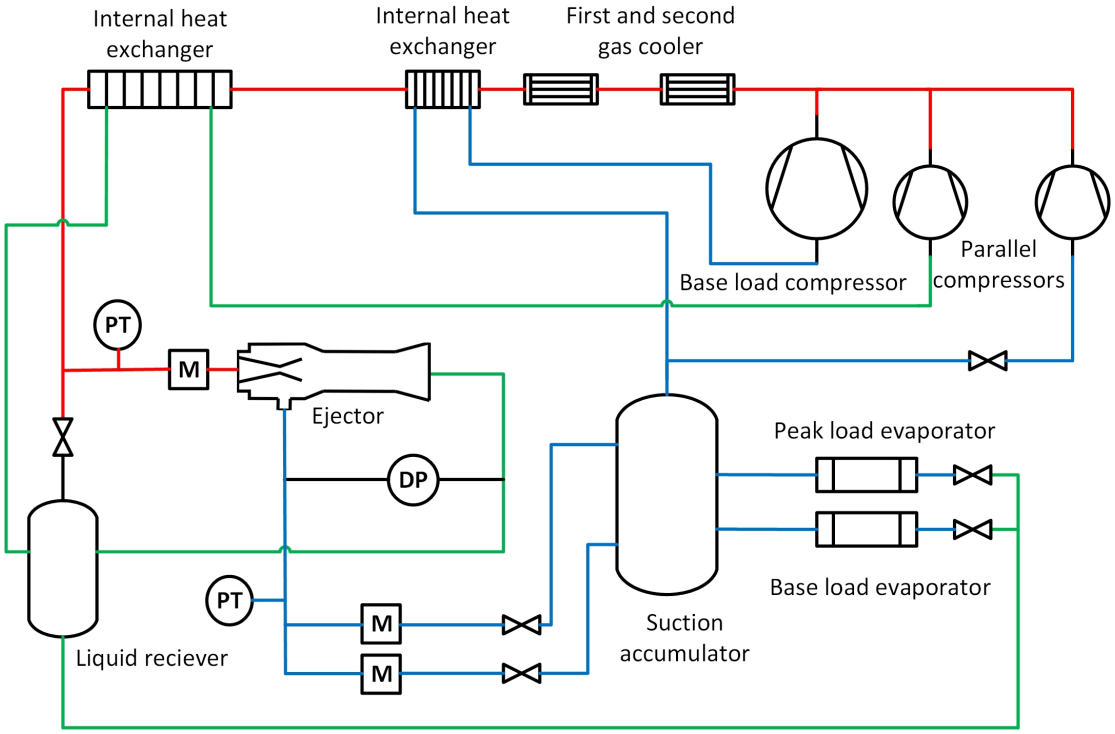

Figure 3. Simplified illustration of the system layout with new ejector and sensors installed. PT—pressure/temperature sensor, DP—differential pressure sensor, M—mass flow meter.

4.2. Comparison with Experimental Results

Four data points will be used for validation of the CFD model corresponding to different motive conditions at 90 bar, 80 bar, 75 bar, and 83 bar and pressure lifts of 2.1 bar, 3.6 bar, 1.5 bar, and 2.5 bar, respectively. These cases will be referred to as cases I-IV and correspond to the experimental data points 49, 59, 62, and 79 in Table A1, respectively. Case I is a measurement at a higher operating pressure and intermediate pressure lift, case II is a measurement at an intermediate operating pressure and high-pressure lift, case III is a measurement at low operating pressure and low-pressure lift, and case IV is a measurement at an intermediate operating pressure and intermediate pressure lift.

The experimental results and the calculated CFD results at those operating conditions are shown in Table 3. Here, the subscripts m, s and o refer to motive, suction and outlet

conditions, respectively. The experimental measurements were calculated from a time series where close to a steady state was achieved. The standard deviation over the measurement period is, therefore, calculated for the mass flow rates and are shown along with the experimental validation data.

Table 3. Comparison of experimental and CFD results at different operating conditions. $\delta = \mathrm{MFR}_{\mathrm{CFD}} - \mathrm{MFR}_{\mathrm{Exp}}$. The MFR measurements are shown with the standard deviation over the experimental measurement period. Subscript *exp* refers to an experimentally obtained value.

	P_m [bar]	T_m [°C]	P_s [bar]	T_s [°C]	P_o [bar]	$MFR_{m,exp}$ [g/s]	δ_m [g/s]	$MFR_{s,exp}$ [g/s]	δ_s [g/s]
I	90.3	29.2	34.2	7.9	36.3	33.9 ± 0.2	−0.9	44.0 ± 0.5	+1.2
II	79.9	29.3	31.9	14.6	35.6	26.0 ± 0.5	−1.5	6.74 ± 0.05	+2.15
III	74.6	24.3	34.3	8.6	35.7	29.3 ± 1.2	−3.6	36.6 ± 1.9	+5.0
IV	82.8	34.5	34.3	9.1	37.0	21.6 ± 0.2	−1.1	26.3 ± 0.7	+13.4

The results from the simulations compared to the experimental data are shown in Table 3. As found previously in the literature [51], a good agreement between experimental measurements and computed solution for the motive MFR is found for the high motive pressure operating conditions, with less than 3%, 6% and 6% difference in predicted MFR for cases I, II, and IV, respectively. As the pressure and temperature are reduced, the motive MFR is underpredicted by −12% by the model in comparison to experimental results, shown in Figure 4. This is in agreement with previous findings with the HEM and is in the literature attributed to non-equilibrium phase change [46].

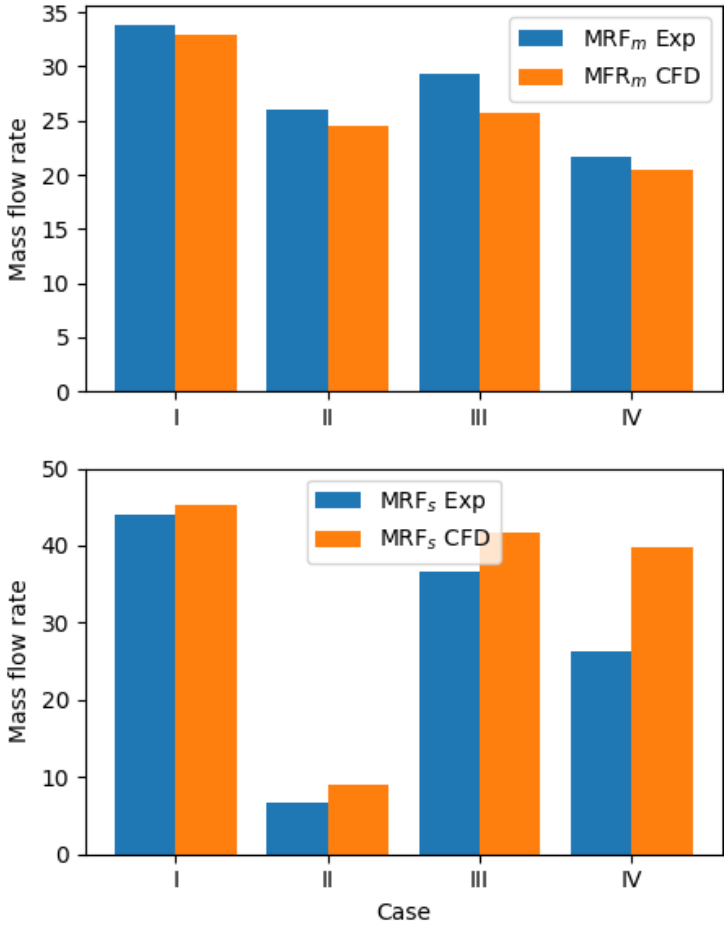

Figure 4. Comparison of experimental and numerical results in terms of motive (**upper**) and suction (**lower**) mass flow rate prediction.

The suction MFR prediction is, in comparison, more challenging to accurately reproduce and the accuracy is, in general, lower than for the motive MFR. Here, the suction MFR is over-predicted by 3%, 31%, 14%, and 51% for cases I, II, III, and IV, respectively. The prediction is thought to be better for the high-pressure cases (I, II) due to the better prediction of the motive flow structure. For the lower pressure case (III), the motive flow structure is less accurately reproduced locally in the ejector, which reduces the prediction accuracy of the mixing process and, therefore, the suction MFR. The suction MFR prediction error is the largest for case IV. Accurate prediction of the suction flow is a common challenge in modeling R744 ejectors, and errors up to 100% are not uncommon. These errors are typically attributed to turbulence modeling; however, currently, there exists no consensus on this [51].

4.3. Mesh Independence Study

A mesh study was conducted to assure that the 3D physics effects are well-presented by the mesh. The four validation points, I, II, III, and IV are calculated using meshes with varied mesh resolutions. Using the ANSYS ICEM software, a 3D-structured mesh was generated with high orthogonal quality and low skewness in the main dimensions. The meshes were generated based on a high-quality in-house meshing algorithm for ejectors, implemented into the ejector CFD automation toolset presented by the author in previous openly available work [57]. This will allow for machine-learning-based optimization of the ejector bypass inlet in future works. An example of the meshes generated is shown in Figure 5. Here, the impact of mesh resolution on the motive flow shock train and the performance parameters is analyzed.

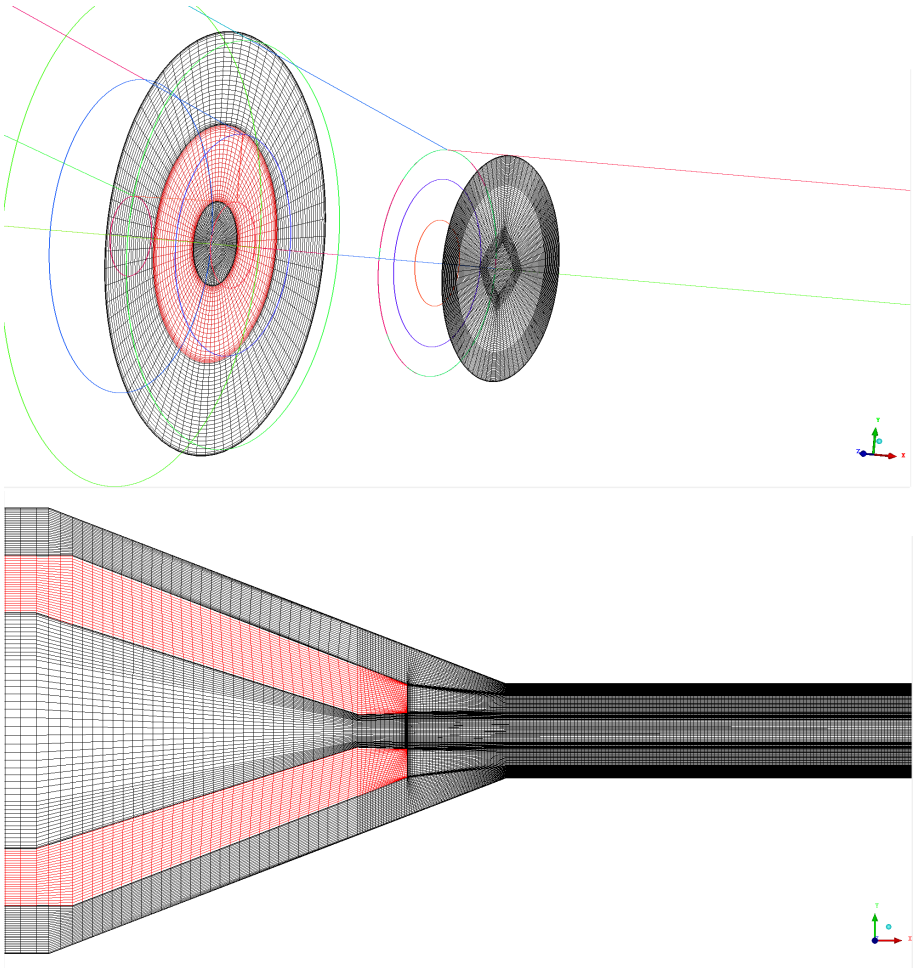

Figure 5. Generic ejector geometry with geometry parameters. The red color signifies solid parts.

Different meshes are compared and referred to as meshes A–E. The meshes A, B, and C were generated with 700,000, 1,000,000, and 2,000,000 cells, respectively. Two additional meshes, D and E, were generated with higher resolution in the premixing chamber and along the ejector walls, respectively. The cell counts for these meshes were 1,400,000 cells for mesh D and 2,500,000 cells for mesh E.

4.3.1. Flow-Rate Prediction

The mesh independence of the mass flow rate prediction must be verified. The motive and suction MFR predicted at different resolutions of mesh quality for the different cases are shown in Table 4. For all cases, the motive mass flow rate prediction is nearly independent of the mesh resolution, and only a 1% overprediction error is found between the coarsest and finest meshes. This is in agreement with previous findings with the HEM [51] and is ascribed to the choked motive flow in the ejector. For all cases, the suction MFR is reduced by increased mesh resolution until reaching around 2000k cells. For case I, the difference between the coarsest and finest mesh in suction MFR prediction is 6%. For cases II and IV the refinement has a large impact on the suction MFR as the mesh is refined to 2,500,000; cells. For mesh E (2,500,000) the accuracy of the suction MFR is, for cases I, II, and III, close to the experimentally obtained data points, and this mesh is concluded to be sufficiently refined for further computation.

Table 4. Mesh convergence study with different mesh sizes.

Mesh	Case	Cells	MFR_m [kg/s]	MFR_s [kg/s]
A	I	700,000	0.0333	0.0473
B	I	1,000,000	0.0331	0.0468
D	I	1,400,000	0.0330	0.0448
E	I	2,500,000	0.0330	0.0452
A	II	700,000	0.0245	0.0105
B	II	1,000,000	0.0245	0.0101
E	II	2,500,000	0.0245	0.0089
A	III	700,000	0.0257	0.0417
B	III	1,000,000	0.0257	0.0417
C	III	2,000,000	0.0257	0.0416
D	IV	1,400,000	0.0205	0.0396
E	IV	2,500,000	0.0206	0.0397

4.3.2. Shock Resolution

The results with meshes A, B, C, and E are compared for the resolution of the motive flow shock train. The pressure distribution along the center ejector axis for case I is shown in Figure 6. Meshes A, B, and C underestimate the shock strength in comparison to mesh E. A more resolved mesh in this region lowers the minimum pressure reached in the shock.

Figure 7 shows the Mach number distribution in the ejector for case IV for two mesh resolutions (1,400,000 and 2,500,000) corresponding to mesh D and E. The Mach number lines for Mach 1 are illustrated with a red contour line. In the figure, it is clear that mesh refinement to 2,500,000 cells improves the detailed resolution of the shock train. The results with mesh E show that the high-velocity core is extended by refining the mesh. This is attributed to the reduction in numerical viscosity from mesh refinement. The difference in predicted mass flow rates is very small, so the effect of this additional resolution does not significantly affect the entrainment of the secondary flow.

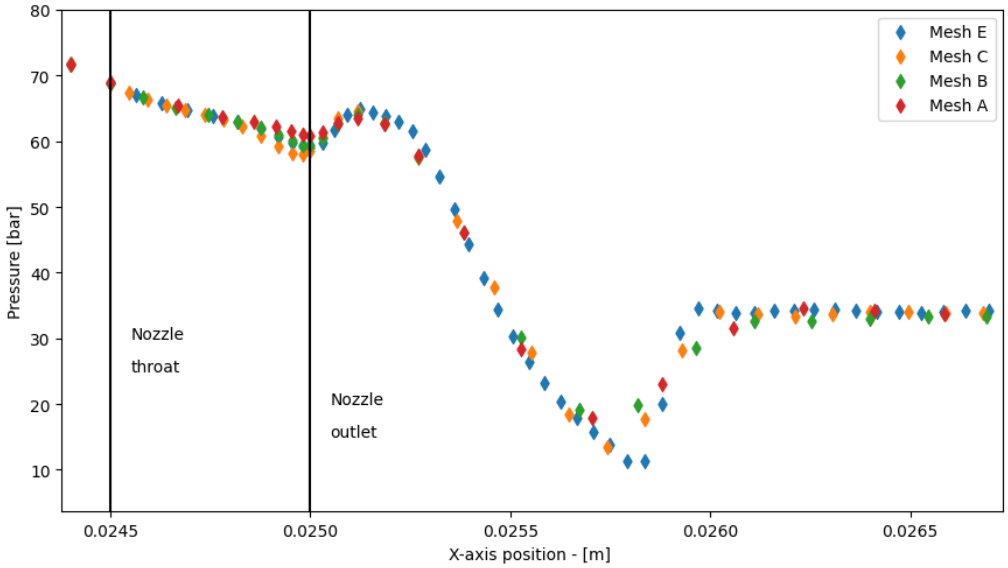

Figure 6. Pressure distribution for case I along the x-axis for meshes A, B, C, and E.

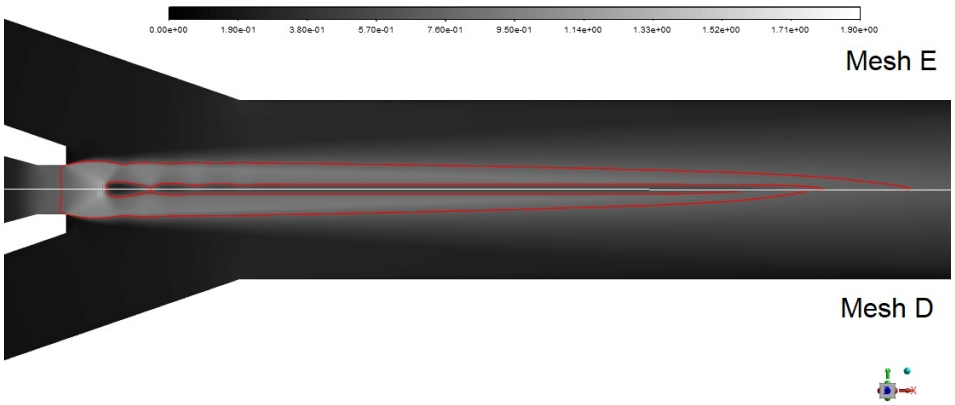

Figure 7. Mach number distribution for meshes E (**top**) and D (**bottom**) for case IV. Red line illustrates Mach 1.

In total, it was decided to use Mesh E with 2,500,000 cells for the following calculations.

4.4. Comparison of Turbulence Models

The choice of turbulence model was based on an initial comparison of the $k-\epsilon$ realizable model and the $k-\omega$ SST model models. A calculation using mesh D for experimental test case I with the two turbulence models was conducted and the results are shown in Table 5.

Table 5. Comparison of turbulence the $k-\omega$ SST and $k-\epsilon$ realizable models for Case I with mesh D.

Turbulence Model	MFR_m [kg/s]	MFR_s [kg/s]
$k-\omega$ SST	0.0330	0.0448
$k-\epsilon$ realizable	0.0330	0.0273
Experimental	0.0339	0.0440

Both models predict the same motive MFR as this is primarily governed by supersonic choking. For prediction of the suction MFR, it is found that the $k-\omega$ model predicts the experimentally measured MFR accurately with an over-prediction error of about 2%. The $k-\epsilon$ model, on the other hand, severely under-predicts the suction MFR with an

error of approximately −38%. This difference in predictive ability could be influenced by many parameters, such as mesh resolution, geometry, and model parameters. In addition, these turbulence models are not tuned for multiphase flows, so these findings are not generalizable outside two-phase R744 ejectors. Still, the findings agree with the detailed turbulence model study of Bodys et al. [50], where the $k-\omega$ model predictions were, overall, more accurate and generally over-predicted the suction MFR, and the $k-\epsilon$ realizable model predictions were overall less accurate and generally under-predicted the suction MFR. Based on these calculations, the authors decided to continue using the $k-\omega$ SST model.

4.5. Bypass Inlet

To verify the importance of meshing and simulating the bypass inlet section, simulations with the bypass inlet section geometrically resolved were compared to simulations with the bypass specified as a boundary on the ejector wall. Introducing the bypass entrance poses a meshing challenge due to the high gradients and large cell skewness near the interception of the mixing chamber and the bypass inlet. Still, simulating the entrance was numerically preferable to specifying the boundary conditions on the ejector wall, as it yielded numerically stable results. Meshing and solution of the bypass entrance region add computational cost to the simulations; however, it also improves the accuracy of the model as a more physically reasonable boundary condition could be specified at the start of the bypass inlet. Furthermore, this removes the need for specifying boundary conditions with specified swirl and axial components, which introduces additional model uncertainties as these components are determined by the bypass inlet geometry.

5. Results

In this work, the swirl-bypass concept is explored by investigating the influence of its main geometry parameters, and their influence on the ejector flow field. First, different swirl-bypass ejector geometries are investigated and discussed regarding optimal design. Secondly, the flow structure and swirl characteristics are explored and analyzed in detail. The simulations are conducted with operating conditions corresponding to case IV and case I. The simulations are set up with boundary conditions for the suction and bypass inlet at the same pressure. The overall performance of the ejector is, therefore, calculated with the total entrainment of the ejector, Equation (2).

In general, the simulations with the bypass inlet showed that gas suction could be achieved; however, the swirl flow would significantly reduce the suction mass flow rate, with a net negative impact on entrainment. This is found in all configurations of geometric design and operating conditions.

The CFD simulations were computed on the NTNU IDUN computing cluster [80]. The cluster has more than 70 nodes and 90 GPUs. Each node contains two Intel Xeon E5-2630 v2 CPUs, at least 128 GB of main memory, and is connected to an Infiniband network. Storage is provided by two storage arrays and a Lustre parallel-distributed file system. Computation time using one 20-core node for a single data point was 1–2 weeks depending on the specific geometry.

5.1. Bypass Inlet Design

A study of the different geometric parameters is conducted. The results are compared to a baseline simulation without a bypass inlet. Due to the large computational cost of each simulation, the study is limited to investigating the swirl-bypass position, the swirl inclination- and tangential angle, and the pressure lift at these two operating conditions. The results are shown in Table 6.

Table 6. Parameter study of the different geometric features of the bypass inlet on bypass performance. Simulations are identified by the simulation ID Sim, where the prefix N indicates no-bypass. The column named Diff is defined as the difference in percentage between the total entrainment (bypass and suction) compared to the same operating condition without bypass.

Case	Sim	x_b [-]	α_i [°]	α_t [°]	P_{lift} [bar]	MFR_s [kg/s]	MFR_b [kg/s]	Diff [%]
Case IV	1	2	0	90	2.5	0.0295	0.0016	−21.3
	2	4	0	90	2.5	0.0321	0.0015	−15.0
	3	7	0	90	2.5	0.0375	0.0006	−3.6
	4	10	0	90	2.5	0.0385	0.0003	−1.8
	5	4	20	90	2.5	0.0324	0.0015	−14.2
	6	4	45	90	2.5	0.0328	0.0012	−13.9
	7	4	0	40	2.5	0.0303	0.0027	−16.5
	8	4	0	60	2.5	0.0308	0.0025	−15.7
	9	4	45	90	2	0.0395	0.0019	−20.0
	10	10	0	90	1	0.0454	0.0025	−14.0
Case I	11	2	0	90	2	0.0328	0.0021	−22.8
	12	4	0	60	2	0.0320	0.0039	−20.6
	13	4	0	90	2	0.0335	0.0021	−21.3
	14	4	20	90	2	0.0340	0.0020	−20.5
	15	7	0	90	2	0.0357	0.0015	−17.7
	16	4	20	90	1	0.0378	0.0024	−18.8
	17	4	20	90	0.5	0.0426	oscillating	
No bypass								
Case IV	N1	-	-	-	2.5	0.039514	-	
	N2	-	-	-	2	0.051762	-	
	N3	-	-	-	1	0.055674	-	
Case I	N4	-	-	-	2	0.045234	-	
	N5	-	-	-	1	0.049482	-	
	N6	-	-	-	0.5	oscillating	-	

5.1.1. Bypass Position, x_b

The first main parameter for a bypass inlet design is the downstream location of the bypass inlet. The bypass locations are defined along the mixing section in increments of mixing chamber diameters. The bypass inlet position was varied between $2 \times D_{\text{mix}}$ and $10 \times D_{\text{mix}}$.

The influence of bypass inlet location is visualized in Figure 8. The figure shows that the choice of inlet bypass position has a major impact on the total pumped flow rate and total entrainment ratio, Equation (2). For a bypass location close to the ejector motive nozzle, the suction effect is more significant, producing a relatively larger bypass flow rate, approximately 1.6 g/s, and 2.1 g/s, for case IV and case IV, respectively. In comparison, the suction nozzle produces 29.5 g/s and 32.8 g/s, for case IV and case IV, respectively. As the bypass port is moved downstream in the mixing chamber, the bypass flow quickly drops to nearly zero. On the other hand, the entrained suction flow increases as the bypass inlet is moved toward the end of the mixing chamber. This is attributed to the bypass flow blocking and disturbing the flow path of the suction flow entering the mixing chamber. Compared to the ejector without a bypass inlet, the effect of the bypass is to reduce the total suction flow as the total flow rate accounted for by the suction nozzle is approximately 10 times larger than the bypass nozzle. This is seen for both operating conditions and all configurations of the bypass port.

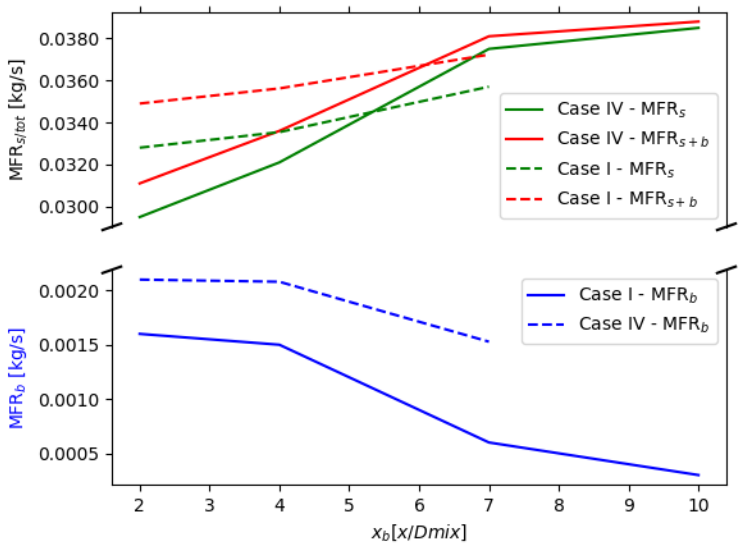

Figure 8. Plot of bypass (blue) and suction (green) mass flow rate as a function of bypass inlet position. The total pumped flow rate is shown in red.

This blockage effect is illustrated in Figure 9. Just after the bypass inlet, colored in blue, the axial velocity through the ejector is reduced to small or even locally negative values. This forces the suction flow that would pass through this area to deviate its flow path, which drastically reduces suction flow. Additionally, the path taken by the suction flow around the bypass flow creates a vortex, illustrated in Figure 10, that disturbs the main motive flow and is moved off-center.

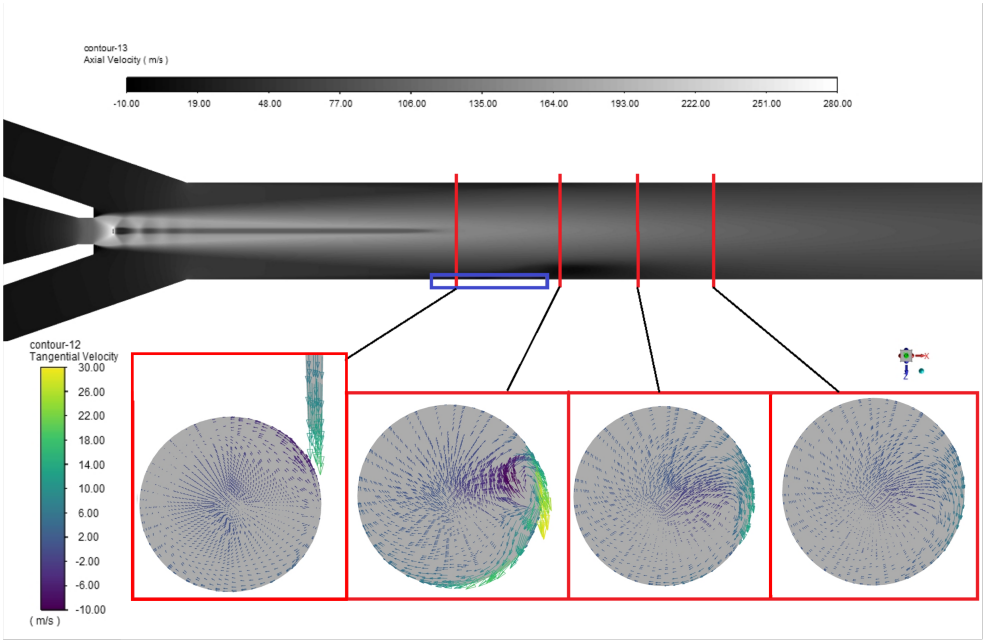

Figure 9. **Top**: Contour plot of the axial velocity in gray. The bypass inlet is colored blue. **Bottom**: Cross-sectional vector plots of the tangential velocity shown for locations along the axial direction after the bypass inlet.

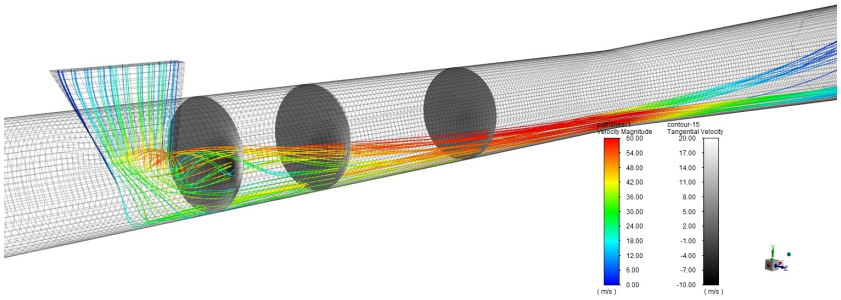

Figure 10. Flowpath illustration of the flow coming from the bypass inlet. Different cross-sectional contour plots of the tangential velocity are shown for locations along the axial direction after the bypass inlet.

5.1.2. Flow Inclination Angle, α_i, and Flow Tangential Angle, α_t

The effect of the flow inclination and tangential angles are evaluated by varying these parameters for the bypass geometry at bypass position $x_b = 4$. The inclination angle is varied between 0° to 45°. The variation in this parameter has only a minor effect on the suction and bypass flow rates. Increasing the flow inclination angle to 20° has a positive impact on the suction flow, increasing it by approximately 1–2% for cases IV and I, and had only a minor negative impact of 4% on the bypass flow for case IV and a negligible impact for case I. Further increasing the inclination angle to 45° further increases the suction mass flow rate by approximately 1%. However, this reduces the bypass flow rate by approximately the same amount. This is in agreement with the findings of Bodys et al. [70], where the impact of the bypass inlet angle was found to be negligible.

Varying the tangential angle of the bypass inlet has a significant impact on both suction and bypass flow. Reducing this angle directs the bypass flow more directly toward the central flow inside the mixing chamber. The central low pressure is, therefore, able to pump more bypass flow into the ejector. However, this comes at the cost of further blocking and disturbing the main suction flow. By decreasing the tangential angle to 60°, the bypass flow rate would increase by 85% for case IV and 66% for case I. Further decreasing this angle to 40° from 60° increased the flow rate by a further 8%. Similarly to the bypass position, the increase in bypass flow rate reduces the suction flow rate. By reducing the tangential bypass angle, the swirl component of the bypass velocity is reduced as the inlet direction is changed from tangential to radial.

5.1.3. Pressure Lift

The effect of varying pressure lift depends on the bypass geometry. For the bypass entrance near the end of the mixing chamber ($x_b = 10$, simulation 4 and 10) the bypass is significantly increased by 730% when the pressure lift is reduced from $P_{\text{lift}} = 2.5$ bar to $P_{\text{lift}} = 1$ bar. While for a bypass entrance close to the start of the mixing chamber ($x_b = 4$, simulation 14 and 16), the influence of the pressure lift on bypass flow rate is smaller, producing only an increase by 20%. Consequently, when the bypass flow is increased at a lower pressure lift, the swirl blockage effect is increased and overall performance is reduced in comparison to the ejector design without a bypass. This is seen for the simulations with a bypass inlet near the end of the ejector mixing chamber, where the difference in total entrainment between an ejector with (simulation 4 and 10) and without (simulation N3) bypass is increased from −1.6% to −14%. However, for bypass inlets near the start of the ejector mixing chamber, this difference is reduced from −20.5% to −18.8%. This increase in performance could be attributed to the higher bypass performance of the bypass inlet for lower pressure lifts. It is noted that the ejector configuration with an inlet further toward the end of the mixing chamber at a low pressure lift corresponds most closely with the conventional bypass ejector design, for instance, discussed by Bodys et al. [70], where the bypass is introduced in the ejector diffuser. However, this configuration is believed to gain less value from increased mixing by introducing a swirl component as the remaining

distance to exploit swirl mixing is shorter. Figure 11 shows the pressure distribution along the mixing-chamber center line. It can be seen that, for higher pressure lift, a significant increase in pressure of approximately 2 bar is seen along the mixing chamber, while only increasing by 0.1 bar in the low-pressure lift case. This implies that the position of the bypass flow rate is more sensitive to the bypass port position for high-pressure-lift operating conditions than for low-pressure lifts. This is important to design for when considering an ejector that will operate at varied pressure lifts.

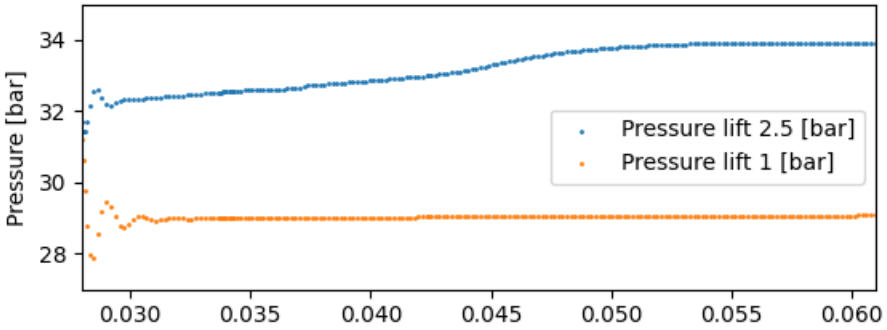

Figure 11. Pressure variation along the mixing-chamber center line for simulations N4 and N5.

5.2. Flow Structure of Swirl Mixing

Plotting the axial velocity distribution (x-direction in figures) along the radial direction at different axial positions in the mixing chamber for simulation N1, the barrel shock flow structure is seen, see Figure 12. The flow structure is symmetric around the ejector center axis. This structure is dampened and smoothed out as the flow moves toward the end of the mixing chamber. At approximately $x_b = 4$, the velocity profile reaches the classical parabolic shape with one velocity maxima along the flow center. These profiles are then used to analyze the boundary layer thickness along the mixing chamber in an ejector without a bypass inlet according to Equation (8), shown in Figure 13. The mixing layer thickness starts very thin with a thickness below 0.1 mm due to the two high-velocity peaks of the barrel shock. As the velocities are decreased, the mixing layer increases to a maximum of 0.9 mm at x_b 8 [-], near halfway through the mixing chamber. The mixing layer then decreases further down the mixing chamber as the velocities are largely evened out.

Referring to the direction towards the bypass entrance (negative z-direction) as angle $\theta_{bp} = 0$, the velocity profiles for the different directions in a swirl-bypass flow is shown in Figure 14 and 15 for simulation 5. Comparing this to the flow structure of the mixing layer without a swirl bypass, it is clear that symmetry is lost. There is a clear low-velocity zone right after the bypass entrance with close to negative axial velocity values, which, as the flow follows the swirl direction path, creates a high-velocity zone on the opposite side of the mixing chamber (θ_{bp} = 180°).

Figure 16 shows the mixing-layer thickness for different directions of velocity profiles calculated based on Equation (8). The mixing-layer thickness has a similar profile to the result without bypass. The figure shows that the mixing layer is for all angles increasing up until a maximum near $x_b = 6$, with a local minimum near $x_b = 4$, the location of the bypass inlet. Near the bypass inlet ($x_b = 4$), as the flow enters and reaches $\theta_{bp} = 90$–$180°$, a low-velocity zone is produced. This low-velocity zone increases the velocity difference between the flow core and the wall, which makes the mixing-layer thickness smaller. The flow that would go through this zone is instead diverted to the region on the opposite side of the bypass inlet, $\theta_{bp} = 270°$, which produces a corresponding high-velocity zone. This high-velocity zone in the suction flow region evens out the flow profile causing the wider mixing layer. As the flow develops down the mixing chamber, these high and low-velocity regions are shifted with the swirling of the flow. Eventually, the high and low flow regions are inverted and the mixing thickness is largest for angle $\theta_{bp} = 90°$ and smallest for the angle $\theta_{bp} = 270°$. The non-symmetric swirl structure then continues further into the diffuser.

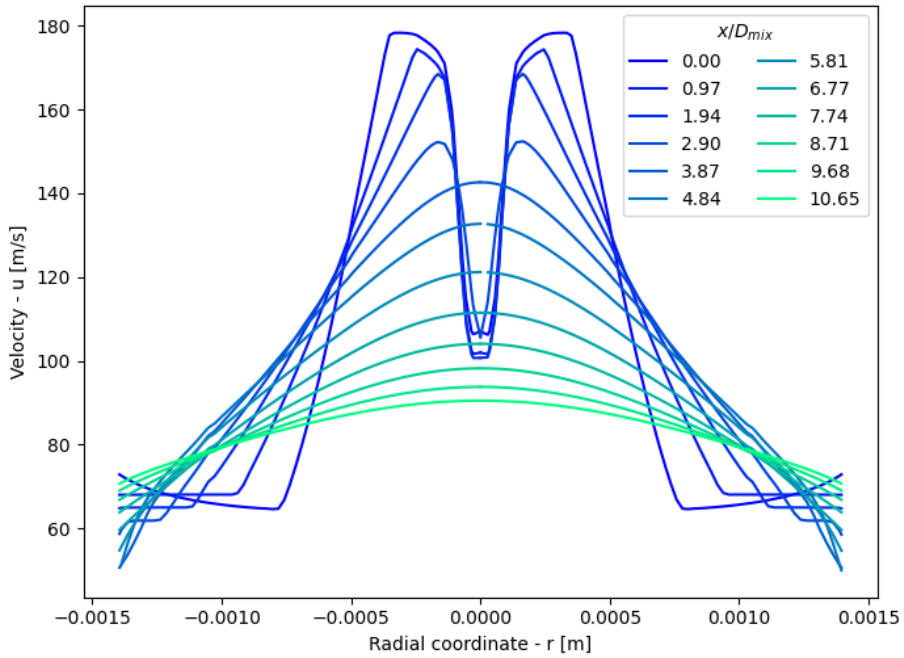

Figure 12. Velocity plot in the y-direction for the ejector without a bypass inlet. The flow is symmetric around the center line in this flow.

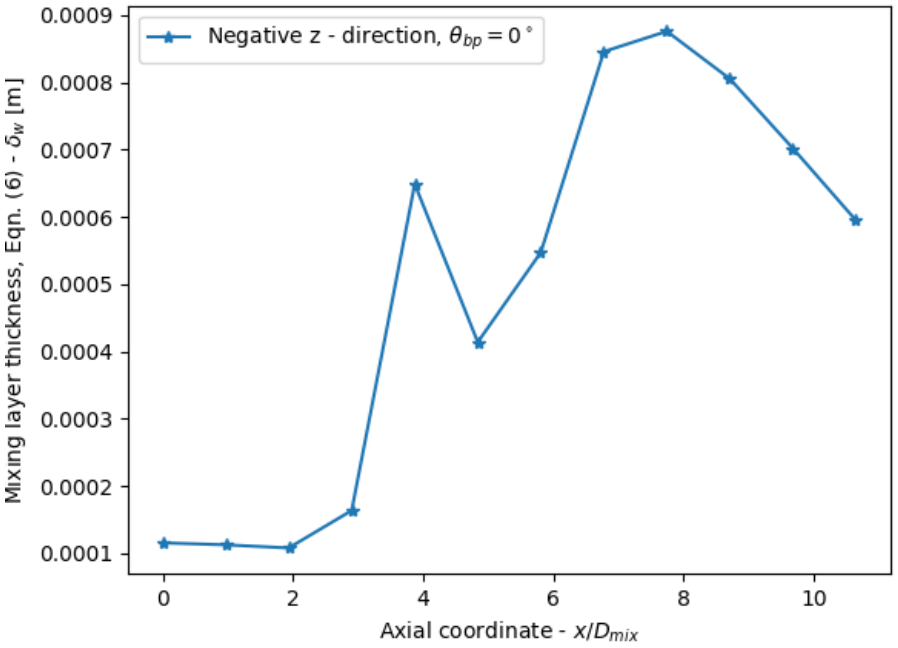

Figure 13. Mixing layer thickness along the mixing-chamber center line without a bypass inlet.

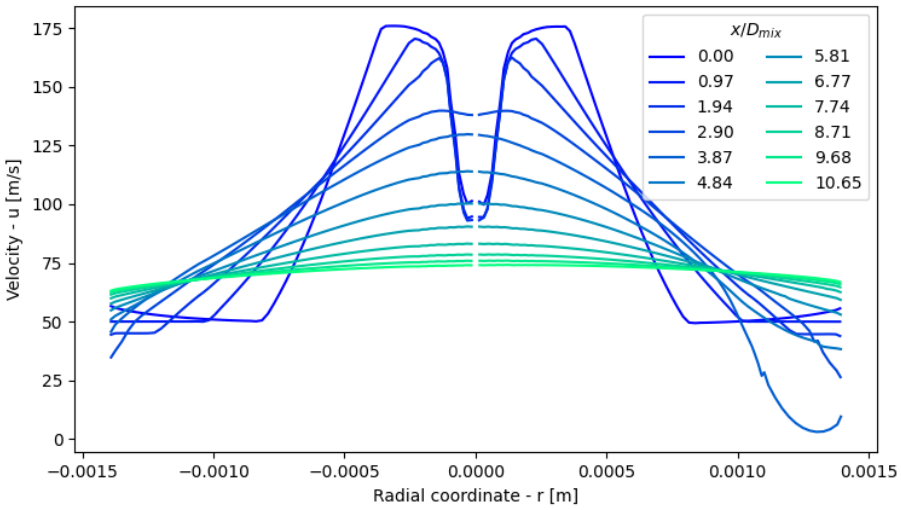

Figure 14. Velocity plot in the z-direction. Positive r direction is in the direction towards the bypass inlet, $\theta_{bp} = 0°$.

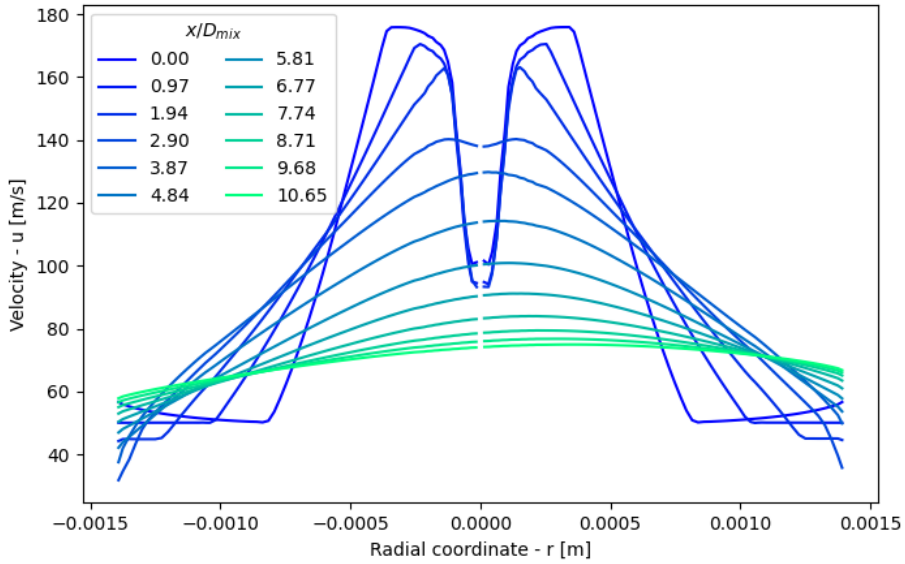

Figure 15. Velocity plot in the y direction. Positive r direction is in the direction furthest offset from the flow path of the bypass inlet, $\theta_{bp} = 270°$.

It is observed that, both for the swirl bypass and the standard ejector geometry, Figures 13 and 16, the mixing-layer thickness is evolving along the mixing chamber. Compared to theoretical estimates of this spreading rate of the mixing layer of a jet [81,82], the spreading rate of the mixing layer in the ejector varies significantly over the ejector mixing chamber. In this figure, no region of steady mixing-thickness growth is available for comparison. This is due to the barrel-shock structure in this ejector, which makes comparison challenging.

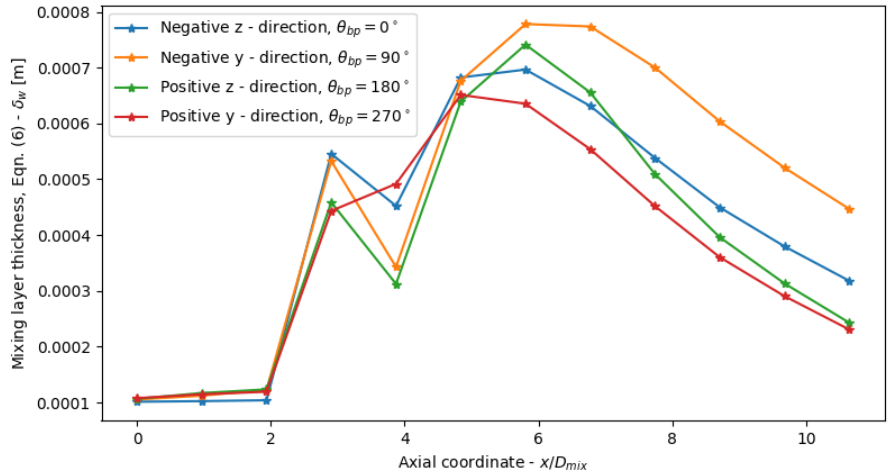

Figure 16. Plot of the mixing-layer thickness for an ejector with a bypass inlet calculated towards the wall in different radial directions plotted along the mixing-chamber center line.

Figures 17 and 18 show the development of the tangential velocity along the different orthogonal radial directions. Figure 17 clearly shows a spike of positive tangential flow near the wall at the starting location of the bypass inlet (positive radial direction). Towards the center, the flow travels in the opposite direction, setting up a vortex that dies out further downstream in the mixing chamber. On the opposing side, the flow tangential-flow direction has evened out over the cross section. In the y direction, Figure 18 shows that, right before the bypass entrance, a significant increase in tangential velocity occurs in the opposing direction to the bypass induced flow. These tangential flows in both positive and negative y directions are both moving away from the bypass inlet and towards the other side of the ejector mixing chamber. This is believed to be caused by the space taken up by the bypass flow displacing the suction flow. Downstream from the bypass inlet, the tangential velocity profile from the bypass flow is established.

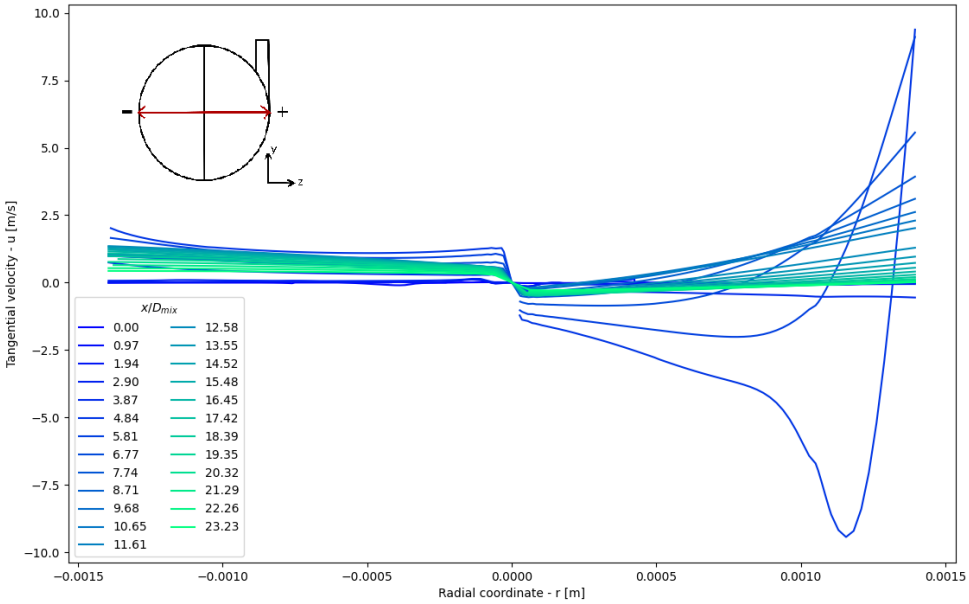

Figure 17. Tangential velocity plot in the z direction. Positive r direction is in the direction towards the bypass inlet, $\theta_{bp} = 0°$.

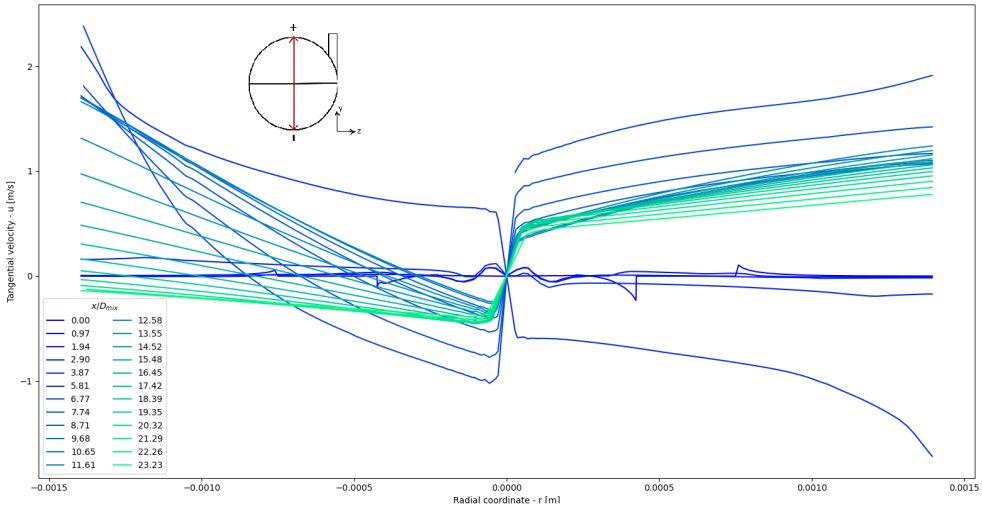

Figure 18. Tangential velocity plot in the y direction. Positive r direction is in the direction furthest offset from the flow path of the bypass inlet, $\theta_{bp} = 270°$.

5.3. Discussion

In this work, the bypass-swirl-generation inlet has been numerically investigated with CFD. The applied HEM CFD model was validated with new experimental results with a new ejector geometry. The results show the highest accuracy for high pressure and temperature motive operating conditions where predictions for motive mass flow rate are within an error 6%, which agree with previous findings in the literature with similar HEM approaches [51]. The validation work presented in this article has highlighted that significant differences are still observed between CFD modeling and measurements. This is especially true for the suction flow, where between 3 and 50% prediction error is observed. This is believed to be due to the local prediction accuracy of motive flow, the lack of accurate turbulence models that account for two-phase effects, and the lack of appropriate multiphase models for this application. In general, the numerical models are limited for high accuracy prediction of the swirl-bypass and suction flow rate. These will depend on the accurate prediction of local flow variables such as pressure and velocities, especially in the vicinity of the bypass inlet. As of yet, very limited local experimental validation data is available for R744 ejectors, primarily due to the small size, high pressures, high velocities, and multiphase flow inside the device. Still, comparison between different models can give valuable insight into the impact of different ejector design variables.

An ejector-bypass concept intended to generate swirl in the ejector mixing chamber is tested for various geometric configurations. The results show that the key impact of the swirl-bypass inlet for this specific ejector geometry is to disturb the suction flow, creating a non-symmetric mixing that reduces ejector performance. This effect is dominant regardless of the bypass angles and position. The main cause of the decrease in performance is attributed to the blocking effect of the bypass flow, limiting the available flow area of the suction flow, the turbulent energy loss induced by the non-optimal collision between these two flows, the lack of swirl component velocity recovery at the outlet, and non-symmetric effects induced by the swirl inlet. Another significant feature of the bypass swirl flow is the non-symmetric flow structure caused by having only one bypass inlet. The non-symmetry caused significant disruption to the flow path of the suction and motive flow that carried on into the diffuser. Based on these simulations, it is found that 3D effects, such as induced non-symmetric flow, are highly important to accurately predict ejector performance with swirl, and that, in general, 2D flow solutions are inadequate for designing such devices.

5.4. Open Access

To promote open access to research into environmentally sustainable solutions with ejectors, the research produced will be made available openly. The ejector geometry, code

for the generation of high-quality ejector swirl bypass mesh in ANSYS ICEM, experimental data, and velocity and mixing layer calculations are available at: https://github.com/knutringstad/Swirl_bypass_ejector (accessed on 10 September 2022).

6. Further Work and Future Design Considerations

Based on the results of this study, several improvements and suggestions for future study of swirl bypass ejectors have been found. The primary reason for the poor performance of the presented ejector is the blockage effect that is caused by the bypass flow obstructing the path of the suction flow. Increasing the diameter of the ejector mixing chamber is believed to allow for the bypass flow to flow primarily in the outer section of the mixing chamber, near the wall. This would reduce the swirl component's radial extension into the suction flow, which, in turn, will reduce the efficiency of the swirl mixing. However, the bigger mixing chamber would allow the suction flow to be less disturbed by the bypass inlet, improving the suction flow rate. Secondly, varying the size and shape of the bypass opening could reduce the impact of the suction flow blocking. Reducing the size of the opening will increase the velocity of the flow from the bypass inlet. This could be applied to intensify mixing while potentially reducing the blocked area of the suction flow. Optimization of the shape of the opening is also of interest; however, for simplicity of component manufacturing rectangular or circular openings are preferred.

Another significant feature of the bypass swirl flow is the non-symmetric flow structure caused by having only one bypass inlet. The non-symmetry caused significant disruption to the flow path of the suction and motive flow that carried on into the diffuser. By increasing the bypass inlet velocity (reducing bypass port flow area) the flow would reach further around the perimeter of the mixing chamber. This could reduce non-symmetry as the bypass flow is more evenly distributed around the mixing chamber axial direction. Another potential design improvement would be to introduce multiple inlets that were offset from each other. Such a solution would reduce non-symmetric effects that push the flow off center. This solution will, however, require additional study to find a good design in terms of manufacturability and port connections.

In this study, the swirl-velocity component is quickly smoothed out by viscosity as the flow progresses through the ejector. However, this effect may be significant for an ejector that produces a larger swirl component. In that case, the diffuser needs to be designed for swirl-component recovery.

Future studies should investigate using a holistic approach to device design. This work has only considered the swirl-bypass inlet as an addition to an already high-performance ejector design. It is, therefore, difficult to gain the largest benefit from the swirl mixing without integrating the bypass port with the other ejector design parameters. This integration could be considered by the use of optimization techniques such as those used in the authors' previous work [57]. The intended application of the swirl bypass inlet is to generate a swirl flow that increases the mixing of motive and suction flow. Each ejector is designed to have this occur inside the mixing chamber. When the pressure lift is lower than design conditions, a higher potential for work recovery is present; however, the mixing chamber will be under-dimensioned for the entrainment ratio. Here, the potential for ejector performance improvement by swirl mixing is the largest. In this work, an ejector designed for already low-pressure lifts was used, so limited improvements could be gained. Future studies should investigate the optimal ranges of swirl mixing operation and these should be integrated into the ejector design. This work has not considered the integration of the bypass and suction port, which should, in general, be designed practically and compactly with limited flow losses. The swirl-bypass concept can also be combined with other ejector concepts. Combining a swirl-bypass and a diffuser-bypass concept could potentially improve ejector entrainment by improving the performance of the ejector under different off-design conditions. Combining motive-inlet swirl and bypass-swirl generation can potentially generate synergistic effects if optimized appropriately to generate additional swirl

flow. Advanced ejector design concepts, especially in combination, require appropriate control strategies for optimal performance, which need to be explored in future work.

The authors also highlight the potential of the second application of a swirl-bypass inlet, referred to in this paper as concept (B), for motive flow control. Such a device has not yet been explored and is left for further work. Most of the design suggestions mentioned are also applicable to such a design. The bypass-design considerations regarding positioning of the bypass inlet for the optimal flow rate are then not applicable, as these are primarily decided by the motive pressure.

7. Conclusions

In this work, a novel swirl-bypass ejector design concept is explored using a high-fidelity 3D CFD model. To verify model accuracy, the multiphase CFD model is validated against new experimental data collected at a range of operating conditions with a novel ejector design. A comparison of experimental and simulation data showed good agreement (within a 6% prediction error) for the motive flow rate prediction for high operating pressures, and poorer agreement (within a 12% prediction error) for lower operating conditions, as is often seen in the literature. The ejector swirl bypass concept performed poorly with a single inlet port. The simulations showed that the generated mixing effect of the swirl flow was minimal in comparison with the reduced efficiency due to the effect of the bypass flow blocking the suction flow area. The reduction in performance of the total entrained flow ranged from -2% to -20%, depending primarily on bypass position. This effect persisted for all different configurations of the bypass port; however, it was lower for bypass positions toward the end of the mixing chamber where less bypass flow rate is produced. The bypass flow rate was found to be highly sensitive to pressure lift for inlets near the end of the mixing chamber, and less sensitive when positioned closer to the motive nozzle. The bypass flow also introduces a non-symmetric effect that pushes the primary and secondary flow out of the ejector center line. This is believed to be causing large losses due to the onset of recirculation zones in the diffuser. The mixing-layer thickness was analyzed with and without the swirl bypass and the off-center motive flow was found to cause the mixing layer between motive and suction flow to be thicker and thinner on either side of the ejector mixing chamber. Lastly, different possibilities for improvements to this concept are suggested that could bring up the efficiency of this ejector design concept. These design improvements include:

- Increase in mixing-chamber diameter.
- Reduction in bypass inlet size.
- Optimization of bypass inlet opening shape.
- Adding additional bypass inlets with a constant offset.

Additionally, several directions for future research have been presented that can potentially improve future generations of the swirl-bypass ejector design:

- Combined design optimization of ejector and swirl bypass inlet.
- Identification of optimal operating ranges.
- Designing for simple and low-cost manufacturing.
- Exploration of the combination of different ejector concepts.
- Definition of appropriate control strategies.

Author Contributions: Conceptualization, K.E.R., A.H., Å.E. and K.B.; methodology, K.E.R., Å.E.; software, K.E.R. and Å.E.; validation, K.E.R. and K.B.; formal analysis, K.E.R.; investigation, K.E.R., A.H., Å.E. and K.B.; resources, K.E.R., A.H., Å.E. and K.B.; data curation, K.E.R. and K.B.; writing—original draft preparation, K.E.R., A.H., Å.E. and K.B.; writing—review and editing, K.E.R., A.H., Å.E. and K.B.; visualization, K.E.R.; supervision, A.H., Å.E. and K.B.; project administration, A.H.; funding acquisition, A.H. All authors have read and agreed to the published version of the manuscript.

Funding: This publication was funded by HighEFF—Centre for an Energy Efficient and Competitive Industry for the Future, an 8-year Research Centre under the FME-scheme (Centre for Environment-friendly Energy Research, 257632). The authors gratefully acknowledge the financial support from the Research Council of Norway and user partners of HighEFF. The authors acknowledge the European Union's Horizon 2020 research and innovation program, 'TRI-HP project' (grant number 814888), for providing the tested ejector and for use of the experimental test rig at NTNU/SINTEF energy research laboratory in Trondheim-Norway.

Institutional Review Board Statement: Not applicable.

Informed Consent Statement: Not applicable.

Data Availability Statement: The data and analysis scripts are available at: https://github.com/knutringstad/Swirl_bypass_ejector (accessed on 10 September 2022).

Conflicts of Interest: The authors declare no conflict of interest.

Appendix A

Table A1. Experimental test data at different pressure and temperature operating conditions at the ejector outlet, suction inlet and motive inlet. The datapoints used in the paper (49, 59, 62, 79) are bolded and marked with an '*'-symbol.

#	P_m [bar]	T_m [°C]	P_m [bar]	T_s [°C]	ΔP [bar]	P_o [bar]	MFR_m [kg/s]	MFR_s [kg/s]
1	79.7	24.7	34.5	14.6	1.5	36.0	0.0322	0.0414
2	79.8	24.1	34.5	9.6	1.9	36.4	0.0331	0.0337
3	80.4	23.1	31.5	9.8	3.9	35.5	0.0346	0.0062
4	85.0	24.2	34.5	13.2	1.6	36.2	0.0361	0.0431
5	84.9	24.4	33.7	11.6	2.0	35.7	0.0357	0.0371
6	85.2	23.7	30.8	9.6	4.3	35.1	0.0368	0.0073
7	89.9	23.8	34.3	10.1	1.7	36.0	0.0390	0.0450
8	90.2	23.9	33.6	9.2	2.0	35.6	0.0391	0.0410
9	90.0	23.4	30.6	8.1	4.6	35.2	0.0395	0.0086
10	94.9	24.4	34.4	9.6	1.8	36.2	0.0409	0.0476
11	95.2	23.5	32.7	8.3	2.8	35.4	0.0418	0.0345
12	95.1	24.1	30.2	7.5	5.2	35.4	0.0414	0.0070
13	65.0	12.0	34.4	12.1	1.2	35.5	0.0315	0.0258
14	69.7	11.5	34.4	11.0	1.0	35.4	0.0342	0.0327
15	74.9	11.9	34.4	9.4	1.0	35.4	0.0367	0.0374
16	65.2	11.9	33.6	13.2	1.9	35.5	0.0319	0.0142
17	70.1	11.7	32.8	9.6	2.4	35.2	0.0348	0.0145
18	74.8	11.9	33.0	8.3	2.1	35.1	0.0370	0.0220
19	64.9	11.9	33.0	16.0	2.5	35.4	0.0321	0.0079
20	70.1	11.9	32.2	9.4	3.0	35.2	0.0352	0.0073
21	75.1	11.9	31.4	8.3	3.7	35.0	0.0379	0.0058
22	65.0	14.5	34.2	13.7	1.3	35.5	0.0311	0.0237
23	69.6	15.4	34.5	11.1	1.1	35.6	0.0331	0.0320
24	74.5	13.5	34.5	10.9	1.1	35.5	0.0361	0.0370
25	64.7	14.6	33.5	13.7	2.0	35.5	0.0312	0.0124
26	70.3	14.8	33.5	11.9	2.1	35.5	0.0340	0.0180
27	74.9	14.4	33.0	9.7	2.1	35.1	0.0365	0.0228
28	64.9	15.3	32.9	14.2	2.6	35.5	0.0315	0.0062
29	69.7	14.8	32.9	14.1	2.8	35.7	0.0339	0.0083
30	75.4	14.6	31.6	9.7	3.5	35.1	0.0373	0.0073
31	70.3	19.1	33.9	10.3	1.6	35.5	0.0324	0.0264
32	74.7	20.3	34.0	12.5	1.2	35.2	0.0340	0.0380
33	80.0	20.0	34.5	10.1	1.2	35.8	0.0369	0.0426

Table A1. *Cont.*

#	P_m [bar]	T_m [°C]	P_m [bar]	T_s [°C]	ΔP [bar]	P_o [bar]	MFR_m [kg/s]	MFR_s [kg/s]
34	85.0	19.3	34.4	9.4	1.2	35.6	0.0394	0.0430
35	90.0	19.2	34.1	7.5	1.3	35.5	0.0415	0.0442
36	94.9	19.5	33.9	7.4	1.5	35.4	0.0434	0.0452
37	69.9	19.3	33.5	11.3	2.0	35.5	0.0320	0.0193
38	75.3	19.0	32.9	11.2	2.3	35.2	0.0354	0.0205
39	80.0	19.2	33.8	9.9	1.9	35.7	0.0373	0.0305
40	85.1	18.8	33.1	8.0	2.2	35.3	0.0398	0.0296
41	89.8	19.3	33.5	6.7	2.0	35.4	0.0415	0.0364
42	94.9	19.7	32.9	7.6	2.4	35.3	0.0435	0.0351
43	70.0	18.6	32.7	16.0	2.8	35.5	0.0328	0.0086
44	75.1	18.4	31.8	11.1	3.5	35.3	0.0360	0.0067
45	79.9	18.8	31.6	11.4	3.9	35.5	0.0380	0.0071
46	84.9	19.2	30.5	6.9	4.4	34.8	0.0404	0.0071
47	89.8	19.4	30.6	8.5	4.8	35.4	0.0423	0.0072
48	95.1	19.1	29.5	6.7	5.4	34.9	0.0447	0.0060
49 *	90.3	29.2	34.2	7.9	2.0	36.3	0.0339	0.0440
50	95.1	28.3	33.8	6.9	2.0	35.8	0.0377	0.0476
51	90.2	29.0	32.4	7.0	3.2	35.6	0.0340	0.0249
52	95.0	28.1	32.5	6.6	3.1	35.6	0.0378	0.0310
53	90.3	29.2	30.8	7.0	4.6	35.5	0.0338	0.0063
54	95.4	27.5	30.3	6.4	5.0	35.3	0.0384	0.0078
55	79.7	28.6	34.4	8.0	1.9	36.3	0.0270	0.0343
56	84.7	30.1	34.5	8.0	2.1	36.6	0.0290	0.0370
57	80.0	29.5	34.8	8.7	2.1	36.9	0.0259	0.0308
58	84.8	28.8	32.4	7.9	3.1	35.5	0.0306	0.0198
59 *	79.9	29.3	31.9	14.6	3.7	35.6	0.0260	0.0067
60	85.1	28.2	30.8	7.0	4.1	34.9	0.0315	0.0076
61	71.2	24.4	34.2	8.8	1.4	35.7	0.0262	0.0336
62 *	74.6	24.3	34.3	8.6	1.5	35.7	0.0293	0.0366
63	69.9	24.6	33.4	9.3	2.2	35.6	0.0247	0.0161
64	75.3	23.7	33.5	8.4	2.1	35.6	0.0305	0.0257
65	69.7	23.4	32.1	9.9	2.9	35.0	0.0266	0.0068
66	74.7	24.4	32.2	13.2	3.3	35.4	0.0291	0.0070
67	72.8	15.2	34.1	11.8	1.3	35.4	0.0350	0.0310
68	73.2	14.7	33.3	11.1	2.0	35.3	0.0355	0.0223
69	72.9	14.8	31.4	10.7	3.5	34.9	0.0363	0.0055
70	80.0	14.8	34.3	9.2	1.1	35.4	0.0384	0.0414
71	79.9	14.1	33.0	8.3	2.2	35.2	0.0388	0.0260
72	80.2	14.1	31.2	8.6	4.1	35.3	0.0397	0.0061
73	80.0	13.9	32.4	8.2	2.9	35.3	0.0391	0.0173
74	85.1	14.6	34.3	10.6	1.2	35.5	0.0407	0.0440
75	84.9	15.1	33.4	9.7	1.9	35.3	0.0406	0.0338
76	85.0	14.2	30.4	8.2	4.6	34.9	0.0420	0.0061
77	79.9	23.7	32.5	8.0	2.8	35.4	0.0335	0.0184
78	84.8	23.9	32.2	7.4	3.1	35.3	0.0364	0.0195
79 *	82.8	34.5	34.3	9.1	2.7	37.0	0.0216	0.0263
80	83.1	34.6	32.4	8.5	3.5	35.9	0.0217	0.0122
81	82.8	34.6	31.7	9.6	3.9	35.6	0.0217	0.0053
82	86.3	34.3	34.4	9.1	2.3	36.7	0.0244	0.0332
83	85.7	34.7	33.4	8.2	3.0	36.4	0.0235	0.0225
84	85.9	33.8	31.3	7.9	4.1	35.3	0.0248	0.0077
85	64.9	19.8	33.9	11.7	1.6	35.5	0.0281	0.0193

Table A1. *Cont.*

#	P_m [bar]	T_m [°C]	P_m [bar]	T_s [°C]	ΔP [bar]	P_o [bar]	MFR_m [kg/s]	MFR_s [kg/s]
86	65.2	19.5	33.5	11.9	2.0	35.5	0.0286	0.0128
87	65.2	19.3	32.6	12.9	2.7	35.3	0.0291	0.0049
88	94.9	19.6	32.2	6.8	3.2	35.4	0.0438	0.0257
89	95.0	19.0	30.9	6.2	4.3	35.2	0.0443	0.0146
90	90.7	18.8	32.1	6.8	3.5	35.5	0.0424	0.0199
91	85.5	19.1	32.1	7.1	3.2	35.3	0.0402	0.0186
92	80.1	18.1	32.2	7.3	3.1	35.2	0.0382	0.0147
93	94.9	13.0	34.2	8.1	1.4	35.6	0.0450	0.0480
94	95.0	12.9	33.0	7.2	2.2	35.2	0.0454	0.0374
95	94.8	12.6	31.9	6.3	3.3	35.1	0.0457	0.0255
96	94.9	12.4	29.4	5.4	5.4	34.7	0.0466	0.0073
97	89.9	12.6	34.2	8.9	1.2	35.4	0.0432	0.0466
98	89.9	12.7	33.1	8.3	2.1	35.2	0.0434	0.0355
99	90.1	12.6	32.1	7.1	3.1	35.2	0.0437	0.0242
100	89.9	12.6	30.5	6.6	4.6	35.1	0.0442	0.0097
101	85.0	12.0	34.3	10.2	1.1	35.5	0.0412	0.0441
102	84.9	12.2	33.0	9.0	2.1	35.1	0.0415	0.0311
103	84.8	12.5	31.9	8.2	3.3	35.1	0.0417	0.0175
104	84.9	12.5	30.5	8.1	4.6	35.0	0.0423	0.0065
105	80.0	12.9	34.1	11.7	1.5	35.6	0.0389	0.0347
106	80.0	12.5	33.4	11.0	2.0	35.4	0.0392	0.0282
107	80.0	12.4	32.2	10.1	3.2	35.3	0.0396	0.0149
108	80.0	11.9	31.0	9.7	4.1	35.1	0.0402	0.0063
109	89.9	12.6	34.2	8.9	1.2	35.4	0.0432	0.0466
110	89.9	12.7	33.1	8.3	2.1	35.2	0.0434	0.0355
111	90.1	12.6	32.1	7.1	3.1	35.2	0.0437	0.0242
112	89.9	12.6	30.5	6.6	4.6	35.1	0.0442	0.0097
113	94.9	13.0	34.2	8.1	1.4	35.6	0.0450	0.0480
114	95.0	12.9	33.0	7.2	2.2	35.2	0.0454	0.0374
115	94.8	12.6	31.9	6.3	3.3	35.1	0.0457	0.0255
116	94.9	12.4	29.4	5.4	5.4	34.7	0.0466	0.0073
117	89.9	14.5	34.0	13.1	1.4	35.4	0.0426	0.0431
118	90.2	14.9	33.1	11.9	2.2	35.3	0.0428	0.0338
119	90.2	14.8	32.1	10.6	3.2	35.3	0.0431	0.0219
120	89.8	14.6	30.1	9.3	5.0	35.0	0.0438	0.0064
121	94.6	14.9	34.1	11.2	1.4	35.6	0.0444	0.0469
122	94.8	14.6	32.7	9.5	2.6	35.2	0.0448	0.0333
123	95.3	14.4	31.7	8.2	3.6	35.2	0.0453	0.0227
124	95.1	14.4	29.8	7.1	5.1	35.0	0.0459	0.0088
125	90.5	33.8	34.4	9.7	2.6	37.0	0.0286	0.0344
126	90.4	33.6	32.5	7.7	3.3	35.8	0.0286	0.0229
127	90.0	33.7	30.9	6.9	4.4	35.3	0.0282	0.0081
128	95.0	33.8	34.1	9.4	2.7	36.8	0.0318	0.0378
129	94.9	34.7	33.1	8.9	3.6	36.7	0.0306	0.0243
130	94.8	33.2	30.8	7.6	4.5	35.3	0.0321	0.0118

References

1. European Commision. Regulation (EU) No 517/2014 of the European Parliament and of the Council of 16th April 2014 on Fluorinated Greenhouse Gases and Repealing Regulation (EC) No 842/2006. *Off. J. Eur. Union* **2014**, *150*, 195–230.
2. Gullo, P.; Hafner, A.; Banasiak, K. Transcritical R744 refrigeration systems for supermarket applications: Current status and future perspectives. *Int. J. Refrig.* **2018**, *93*, 269–310. [CrossRef]
3. Karampour, M.; Sawalha, S. Energy efficiency evaluation of integrated CO_2 trans-critical system in supermarkets: A field measurements and modelling analysis. *Int. J. Refrig.* **2017**, *82*, 470–486. [CrossRef]
4. Rony, R.; Yang, H.; Krishnan, S.; Song, J.; Rony, R.U.; Yang, H.; Krishnan, S.; Song, J. Recent Advances in Transcritical CO_2 (R744) Heat Pump System: A Review. *Energies* **2019**, *12*, 457. [CrossRef]
5. Austin, B.T.; Sumathy, K. Transcritical carbon dioxide heat pump systems: A review. *Renew. Sustain. Energy Rev.* **2011**, *15*, 4013–4029. [CrossRef]

6. Jin, Z.; Eikevik, T.M.; Nekså, P.; Hafner, A. Investigation on CO_2 hybrid ground-coupled heat pumping system under warm climate. *Int. J. Refrig.* **2016**, *62*, 145–152. [CrossRef]
7. Yang, J.; Yu, B.; Chen, J. Improved genetic algorithm-based prediction of a CO_2 micro-channel gas-cooler against experimental data in automobile air conditioning system. *Int. J. Refrig.* **2019**, *106*, 517–525. [CrossRef]
8. Luger, C.; Rieberer, R. Multi-objective design optimization of a rail HVAC CO_2 cycle. *Int. J. Refrig.* **2018**, *92*, 133–142. [CrossRef]
9. Ozcana, H.G.; Gunerhanb, H.; Hepbaslia, A.; Yaldirakc, H. Environmental Impact and Performance Comparison of Refrigerants (R744 and R134a) in a Mobile Air Conditioning System Used for Cooling Buses. *Int. J. Eng. Technol.* **2014**, *7*, 233–241. [CrossRef]
10. de Carvalho, B.Y.K.; Melo, C.; Pereira, R.H. An experimental study on the use of variable capacity two-stage compressors in transcritical carbon dioxide light commercial refrigerating systems. *Int. J. Refrig.* **2019**, *106*, 604–615. [CrossRef]
11. Mastrullo, R.; Mauro, A.W.; Perrone, A. A model and simulations to investigate the effects of compressor and fans speeds on the performance of CO_2 light commercial refrigerators. *Appl. Therm. Eng.* **2015**, *84*, 158–169. [CrossRef]
12. Sian, R.A.; Wang, C.C. Comparative study for CO_2 and R-134a heat pump tumble dryer—A rational approach. *Int. J. Refrig.* **2019**, *106*, 474–491. [CrossRef]
13. Mancini, F.; Minetto, S.; Fornasieri, E. Thermodynamic analysis and experimental investigation of a CO_2 household heat pump dryer. *Int. J. Refrig.* **2011**, *34*, 851–858. [CrossRef]
14. Purohit, N.; Sharma, V.; Fricke, B.; Gupta, D.K.; Dasgupta, M.S. Parametric analysis and optimization of CO_2 trans-critical cycle for chiller application in a warm climate. *Appl. Therm. Eng.* **2019**, *150*, 706–719. [CrossRef]
15. Dai, B.; Zhao, X.; Liu, S.; Yang, Q.; Zhong, D.; Hao, Y.; Hao, Y. Energetic, exergetic and exergoeconomic assessment of transcritical CO_2 reversible system combined with dedicated mechanical subcooling (DMS) for residential heating and cooling. *Energy Convers. Manag.* **2020**, *209*, 112594. [CrossRef]
16. Smitt, S.; Tolstorebrov, I.; Gullo, P.; Pardiñas, A.; Hafner, A. Energy use and retrofitting potential of heat pumps in cold climate hotels. *J. Clean. Prod.* **2021**, *298*, 126799. [CrossRef]
17. Kim, M.H.; Pettersen, J.; Bullard, C.W. Fundamental process and system design issues in CO_2 vapor compression systems. *Prog. Energy Combust. Sci.* **2004**, *30*, 119–174. [CrossRef]
18. Gullo, P.; Hafner, A.; Banasiak, K.; Minetto, S.; Kriezi, E.; Gullo, P.; Hafner, A.; Banasiak, K.; Minetto, S.; Kriezi, E.E. Multi-Ejector Concept: A Comprehensive Review on its Latest Technological Developments. *Energies* **2019**, *12*, 406. [CrossRef]
19. Elbel, S.; Lawrence, N. Review of recent developments in advanced ejector technology. *Int. J. Refrig.* **2016**, *62*, 1–18. [CrossRef]
20. Chen, J.; Jarall, S.; Havtun, H.; Palm, B. A review on versatile ejector applications in refrigeration systems. *Renew. Sustain. Energy Rev.* **2015**, *49*, 67–90. [CrossRef]
21. Sumeru, K.; Nasution, H.; Ani, F.N. A review on two-phase ejector as an expansion device in vapor compression refrigeration cycle. *Renew. Sustain. Energy Rev.* **2012**, *16*, 4927–4937. [CrossRef]
22. Sarkar, J. Ejector enhanced vapor compression refrigeration and heat pump systems - A review. *Renew. Sustain. Energy Rev.* **2012**, *16*, 6647–6659. [CrossRef]
23. Besagni, G.; Mereu, R.; Inzoli, F. Ejector refrigeration: A comprehensive review. *Renew. Sustain. Energy Rev.* **2016**, *53*, 373–407. [CrossRef]
24. Tashtoush, B.M.; Al-Nimr, M.A.; Khasawneh, M.A. A comprehensive review of ejector design, performance, and applications. *Appl. Energy* **2019**, *240*, 138–172. [CrossRef]
25. Aidoun, Z.; Ameur, K.; Falsafioon, M.; Badache, M.; Aidoun, Z.; Ameur, K.; Falsafioon, M.; Badache, M. Current Advances in Ejector Modeling, Experimentation and Applications for Refrigeration and Heat Pumps. Part 2: Two-Phase Ejectors. *Inventions* **2019**, *4*, 16. [CrossRef]
26. Elbel, S. Historical and present developments of ejector refrigeration systems with emphasis on transcritical carbon dioxide air-conditioning. *Int. J. Refrig.* **2011**, *34*, 1545–1561. [CrossRef]
27. Besagni, G. Ejectors on the cutting edge: The past, the present and the perspective. *Energy* **2019**, *170*, 998–1003. [CrossRef]
28. Bodys, J.; Palacz, M.; Haida, M.; Smolka, J.; Nowak, A.J.; Banasiak, K.; Hafner, A. Full-scale multi-ejector module for a carbon dioxide supermarket refrigeration system: Numerical study of performance evaluation. *Energy Convers. Manag.* **2017**, *138*, 312–326. [CrossRef]
29. Nakagawa, M.; Marasigan, A.; Matsukawa, T.; Kurashina, A. Experimental investigation on the effect of mixing length on the performance of two-phase ejector for CO_2 refrigeration cycle with and without heat exchanger. *Int. J. Refrig.* **2011**, *34*, 1604–1613. [CrossRef]
30. Zhu, J.; Elbel, S. Application of Vortex Control to an Automotive Transcritical R744 Ejector Cycle. *SAE Tech. Pap. Ser.* **2018**, *1*, 1–6. [CrossRef]
31. Zheng, L.; Deng, J.; Zhang, Z. Dynamic simulation of an improved transcritical CO_2 ejector expansion refrigeration cycle. *Energy Convers. Manag.* **2016**, *114*, 278–289. [CrossRef]
32. Liu, F.; Groll, E.A. Study of ejector efficiencies in refrigeration cycles. *Appl. Therm. Eng.* **2013**, *52*, 360–370. [CrossRef]
33. Elbel, S.; Hrnjak, P. Experimental validation of a prototype ejector designed to reduce throttling losses encountered in transcritical R744 system operation. *Int. J. Refrig.* **2008**, *31*, 411–422. [CrossRef]
34. Taslimi Taleghani, S.; Sorin, M.; Poncet, S.; Nesreddine, H. Performance investigation of a two-phase transcritical CO_2 ejector heat pump system. *Energy Convers. Manag.* **2019**, *185*, 442–454. [CrossRef]

35. Taslimi Taleghani, S.; Sorin, M.; Poncet, S. Modeling of two-phase transcritical CO_2 ejectors for on-design and off-design conditions. *Int. J. Refrig.* **2018**, *87*, 91–105. [CrossRef]
36. Smolka, J.; Bulinski, Z.; Fic, A.; Nowak, A.J.; Banasiak, K.; Hafner, A. A computational model of a transcritical R744 ejector based on a homogeneous real fluid approach. *Appl. Math. Model.* **2013**, *37*, 1208–1224. [CrossRef]
37. Lucas, C.; Rusche, H.; Schroeder, A.; Koehler, J. Numerical investigation of a two-phase CO_2 ejector. *Int. J. Refrig.* **2014**, *43*, 154–166. [CrossRef]
38. Palacz, M.; Smolka, J.; Kus, W.; Fic, A.; Bulinski, Z.; Nowak, A.J.; Banasiak, K.; Hafner, A. CFD-based shape optimisation of a CO_2 two-phase ejector mixing section. *Appl. Therm. Eng.* **2016**, *95*, 62–69. [CrossRef]
39. Palacz, M.; Smolka, J.; Nowak, A.J.; Banasiak, K.; Hafner, A. Shape optimisation of a two-phase ejector for CO_2 refrigeration systems. *Int. J. Refrig.* **2017**, *74*, 210–221. [CrossRef]
40. Haida, M.; Smolka, J.; Hafner, A.; Ostrowski, Z.; Palacz, M.; Madsen, K.B.; Försterling, S.; Nowak, A.J.; Banasiak, K. Performance mapping of the R744 ejectors for refrigeration and air conditioning supermarket application: A hybrid reduced-order model. *Energy* **2018**, *153*, 933–948. [CrossRef]
41. Fang, Y.; Poncet, S.; Nesreddine, H.; Bartosiewicz, Y. An open-source density-based solver for two-phase CO_2 compressible flows: Verification and validation. *Int. J. Refrig.* **2019**, *106*, 526–538. [CrossRef]
42. Haida, M.; Fingas, R.; Szwajnoch, W.; Smolka, J.; Palacz, M.; Bodys, J.; Nowak, A.; Haida, M.; Fingas, R.; Szwajnoch, W.; et al. An Object-Oriented R744 Two-Phase Ejector Reduced-Order Model for Dynamic Simulations. *Energies* **2019**, *12*, 1282. [CrossRef]
43. He, Y.; Deng, J.; Li, Y.; Ma, L. A numerical contrast on the adjustable and fixed transcritical CO_2 ejector using exergy flux distribution analysis. *Energy Convers. Manag.* **2019**, *196*, 729–738. [CrossRef]
44. He, Y.; Deng, J.; Li, Y.; Zhang, X. Synergistic effect of geometric parameters on CO_2 ejector based on local exergy destruction analysis. *Appl. Therm. Eng.* **2021**, *184*, 116256. [CrossRef]
45. Colarossi, M.; Trask, N.; Schmidt, D.P.; Bergander, M.J. Multidimensional modeling of condensing two-phase ejector flow. *Int. J. Refrig.* **2012**, *35*, 290–299. [CrossRef]
46. Palacz, M.; Haida, M.; Smolka, J.; Nowak, A.J.; Banasiak, K.; Hafner, A. HEM and HRM accuracy comparison for the simulation of CO_2 expansion in two-phase ejectors for supermarket refrigeration systems. *Appl. Therm. Eng.* **2017**, *115*, 160–169. [CrossRef]
47. Bodys, J.; Smolka, J.; Palacz, M.; Haida, M.; Banasiak, K. Non-equilibrium approach for the simulation of CO_2 expansion in two-phase ejector driven by subcritical motive pressure. *Int. J. Refrig.* **2020**, *114*, 32–46. [CrossRef]
48. Giacomelli, F.; Mazzelli, F.; Milazzo, A. A novel CFD approach for the computation of R744 flashing nozzles in compressible and metastable conditions. *Energy* **2018**, *162*, 1092–1105. [CrossRef]
49. Giacomelli, F.; Mazzelli, F.; Banasiak, K.; Hafner, A.; Milazzo, A. Experimental and computational analysis of a R744 flashing ejector. *Int. J. Refrig.* **2019**, *107*, 326–343. [CrossRef]
50. Bodys, J.; Smolka, J.; Palacz, M.; Haida, M.; Banasiak, K.; Nowak, A.J. Effect of turbulence models and cavitation intensity on the motive and suction nozzle mass flow rate prediction during a non-equilibrium expansion process in the CO_2 ejector. *Appl. Therm. Eng.* **2022**, *201*, 117743. [CrossRef]
51. Ringstad, K.E.; Allouche, Y.; Gullo, P.; Ervik, Å.; Banasiak, K.; Hafner, A. A detailed review on CO_2 two-phase ejector flow modeling. *Therm. Sci. Eng. Prog.* **2020**, *20*, 100647. [CrossRef]
52. Nowak, A.J.; Palacz, M.; Smolka, J.; Banasiak, K.; Bulinski, Z.; Fic, A.; Hafner, A. CFD simulations of transport phenomena during transcritical flow of real fluid (CO_2) within ejector. *Int. J. Numer. Methods Heat Fluid Flow* **2016**, *26*, 805–817. [CrossRef]
53. Zhu, Y.; Wang, Z.; Yang, Y.; Jiang, P.X. Flow visualization of supersonic two-phase transcritical flow of CO_2 in an ejector of a refrigeration system. *Int. J. Refrig.* **2017**, *74*, 352–359. [CrossRef]
54. Bodys, J.; Palacz, M.; Haida, M.; Smolka, J.; Dziurowicz, D.; Majchrzyk, M.; Nowak, A.J. Experimental investigation of R744 transcritical flow and mixing in the two-phase ejector. *J. Physics: Conf. Ser.* **2022**, *2177*, 012044. [CrossRef]
55. Palacz, M.; Bodys, J.; Haida, M.; Smolka, J.; Nowak, A.J. Two-phase flow visualisation in the R744 vapour ejector for refrigeration systems. *Appl. Therm. Eng.* **2022**, *210*, 118322. [CrossRef]
56. Banasiak, K.; Hafner, A.; Andresen, T. Experimental and numerical investigation of the influence of the two-phase ejector geometry on the performance of the R744 heat pump. *Int. J. Refrig.* **2012**, *35*, 1617–1625. [CrossRef]
57. Ringstad, K.E.; Banasiak, K.; Ervik, Å.; Hafner, A. Machine learning and CFD for mapping and optimization of CO_2 ejectors. *Appl. Therm. Eng.* **2021**, *199*, 117604. [CrossRef]
58. Lucas, C.; Koehler, J. Experimental investigation of the COP improvement of a refrigeration cycle by use of an ejector. *Int. J. Refrig.* **2012**, *35*, 1595–1603. [CrossRef]
59. Gullo, P.; Kærn, M.R.; Haida, M.; Smolka, J.; Elbel, S. A Review on Current Status of Capacity Control Techniques for Two-Phase Ejectors. *Int. J. Refrig.* **2020**, *119*, 64–79. [CrossRef]
60. Hafner, A.; Försterling, S.; Banasiak, K. Multi-ejector concept for R-744 supermarket refrigeration. *Int. J. Refrig.* **2014**, *43*, 1–13. [CrossRef]
61. Zhu, J.; Elbel, S. Experimental investigation of a novel expansion device control mechanism: Vortex control of initially subcooled flashing R134a flow expanded through convergent-divergent nozzles. *Int. J. Refrig.* **2018**, *85*, 167–183. [CrossRef]
62. Liu, F.; Groll, E.A.; Li, D. Investigation on performance of variable geometry ejectors for CO_2 refrigeration cycles. *Energy* **2012**, *45*, 829–839. [CrossRef]

63. Gullo, P.; Birkelund, M.; Kriezi, E.E.; Ryhl Kærn, M. Novel flow modulation method for R744 two-phase ejectors—Proof of concept, optimization and first experimental results. *Energy Convers. Manag.* **2021**, *237*, 114082. [CrossRef]
64. Tang, Y.; Liu, Z.; Li, Y.; Shi, C.; Wu, H. Performance improvement of steam ejectors under designed parameters with auxiliary entrainment and structure optimization for high energy efficiency. *Energy Convers. Manag.* **2017**, *153*, 12–21. [CrossRef]
65. Tang, Y.; Li, Y.; Liu, Z.; Wu, H.; Fu, W. A novel steam ejector with auxiliary entrainment for energy conservation and performance optimization. *Energy Convers. Manag.* **2017**, *148*, 210–221. [CrossRef]
66. Chen, W.; Huang, C.; Chong, D.; Yan, J.J. Numerical assessment of ejector performance enhancement by means of combined adjustable-geometry and bypass methods. *Appl. Therm. Eng.* **2019**, *149*, 950–959. [CrossRef]
67. Chen, W.; Fan, J.; Huang, C.; Liu, S.; Chong, D.; Yan, J.J. Numerical assessment of ejector performance enhancement by means of two-bypass inlets. *Appl. Therm. Eng.* **2020**, *171*, 115086. [CrossRef]
68. Chen, W.; Chen, H.; Shi, C.; Xue, K.; Chong, D.T.; Yan, J.J. Impact of operational and geometrical factors on ejector performance with a bypass. *Appl. Therm. Eng.* **2016**, *99*, 476–484. [CrossRef]
69. Chen, W.; Chen, H.; Shi, C.; Xue, K.; Chong, D.; Yan, J. A novel ejector with a bypass to enhance the performance. *Appl. Therm. Eng.* **2016**, *93*, 939–946. [CrossRef]
70. Bodys, J.; Smolka, J.; Banasiak, K.; Palacz, M.; Haida, M.; Nowak, A.J. Performance improvement of the R744 two-phase ejector with an implemented suction nozzle bypass. *Int. J. Refrig.* **2018**, *90*, 216–228. [CrossRef]
71. Bodys, J.; Smolka, J.; Palacz, M.; Haida, M.; Banasiak, K.; Nowak, A.J. Experimental and numerical study on the R744 ejector with a suction nozzle bypass. *Appl. Therm. Eng.* **2021**, *194*, 117015. [CrossRef]
72. Park, I.S. Numerical investigation of entraining performance and operational robustness of thermal vapor compressor having swirled motive steam inflow. *Desalination* **2010**, *257*, 206–211. [CrossRef]
73. Bodys, J.; Smolka, J.; Palacz, M.; Haida, M.; Banasiak, K.; Nowak, A.J.; Hafner, A. Performance of fixed geometry ejectors with a swirl motion installed in a multi-ejector module of a CO_2 refrigeration system. *Energy* **2016**, *117*, 620–631. [CrossRef]
74. Bell, I.H.; Wronski, J.; Quoilin, S.; Lemort, V. Pure and Pseudo-pure Fluid Thermophysical Property Evaluation and the Open-Source Thermophysical Property Library CoolProp. *Ind. Eng. Chem. Res.* **2014**, *53*, 2498–2508. [CrossRef] [PubMed]
75. ANSYS. ANSYS Fluent Theory Guide. Release 19.0. Canonsburg. 2018. Available online: https://www.ansys.com/academic/terms-and-conditions (accessed on 10 September 2022).
76. Gatski, T.B.; Bonnet, J.P. *Compressibility, Turbulence and High Speed Flow*; Elsevier Ltd.: Amsterdam, The Netherlands, 2013. [CrossRef]
77. Palacz, M.; Smolka, J.; Fic, A.; Bulinski, Z.; Nowak, A.J.; Banasiak, K.; Hafner, A. Application range of the HEM approach for CO_2 expansion inside two-phase ejectors for supermarket refrigeration systems. *Int. J. Refrig.* **2015**, *59*, 251–258. [CrossRef]
78. Banasiak, K.; Hafner, A.; Kriezi, E.E.; Madsen, K.B.; Birkelund, M.; Fredslund, K.; Olsson, R. Development and performance mapping of a multi-ejector expansion work recovery pack for R744 vapour compression units. *Int. J. Refrig.* **2015**, *57*, 265–276. [CrossRef]
79. Banasiak, K.; Hafner, A. 1D Computational model of a two-phase R744 ejector for expansion work recovery. *Int. J. Therm. Sci.* **2011**, *50*, 2235–2247. [CrossRef]
80. Sjalander, M.; Jahre, M.; Tufte, G.; Reissmann, N. {EPIC}: An Energy-Efficient, High-Performance {GPGPU} Computing Research Infrastructure. *arXiv* **2019**, arXiv:1912.05848.
81. Brown, G.L.; Roshko, A. On density effects and large structure in turbulent mixing layers. *J. Fluid Mech.* **1974**, *64*, 775–816. [CrossRef]
82. Papamoschou, D.; Roshko, A. The compressible turbulent shear layer: An experimental study. *J. Fluid Mech.* **1988**, *197*, 453–477. [CrossRef]